# EFFECT OF COUDÉ PUPIL ROTATION ON SODIUM LASER BEACON PERSPECTIVE ELONGATION

THESIS

Russell McGuigan, Flight Lieutenant, RAAF

AFIT/GE/ENG/11-28

**DEPARTMENT OF THE AIR FORCE**
**AIR UNIVERSITY**

## AIR FORCE INSTITUTE OF TECHNOLOGY

**Wright-Patterson Air Force Base, Ohio**

AFIT/GE/ENG/11-28

EFFECT OF COUDÉ PUPIL ROTATION ON SODIUM LASER BEACON
PERSPECTIVE ELONGATION

THESIS

Presented to the Faculty

Department of Electrical and Computer Engineering

Graduate School of Engineering and Management

Air Force Institute of Technology

Air University

Air Education and Training Command

in Partial Fulfillment of the Requirements for the

Degree of Master of Science in Electrical Engineering

Russell McGuigan, B.Eng (Elec)

Flight Lieutenant, RAAF

March 2011

AFIT/GE/ENG/11-28

EFFECT OF COUDÉ PUPIL ROTATION ON SODIUM LASER BEACON

PERSPECTIVE ELONGATION

Russell McGuigan, B.Eng (Elec)
Flight Lieutenant, RAAF

Approved:

| //signed// | March 2011 |
|---|---|
| Jason D. Schmidt (Chairman) | Date |
| //signed// | March 2011 |
| Salvatore J. Cusumano (Member) | Date |
| //signed// | March 2011 |
| Steven T. Fiorino (Member) | Date |

AFIT/GE/ENG/11-28

# Abstract

The use of sodium laser beacons in adaptive optics is relatively novel, and there is much current research in this field. Perspective elongation is a side effect of using these beacons, and results in a different shaped beacon viewed by each subaperture, depending on its location with relative to the laser. Typical calibration of wavefront sensors assumes that each subaperture image is identical, reducing accuracy.

Unfortunately, telescopes built with a Coudé path have a rotating exit pupil that rotates when the telescope elevation or azimuth changes. This rotation ensures that static calibration of the sensor with a single elongated reference beacon is inadequate, and a different approach is required.

This research models the sodium beacon, its transmission through the atmosphere and its measurement by a Shack-Hartmann wavefront sensor (SHWFS). By predicting the extent of beacon elongation and Coudé rotation, it is possible to produce reference images for each subaperture throughout an engagement scenario. These reference sources are then used to continuously recalibrate the system as it changes orientation.

This model measures the effect of perspective elongation and Coudé on SHWFS measurements to quantitatively determine the extent of degradation that occurs. It also predicts the improvement that could be achieved by considering these effects, and allows comparisons between alternate system configurations. From the computer model, it was determined that accounting for perspective elongation and rotation can reduce errors in measurements by up to 50% in a typical scenario.

# Acknowledgements

First and foremost, I would like to offer my sincere thanks to Maj. Jason Schmidt for his willingness to take me on as a student and for sharing his extensive knowledge in adaptive optics and computer simulations. He has continually been a great mentor and I am grateful that I was able to work with such a dedicated and talented advisor. I would like to extend this appreciation to my committee members, Dr. Salvatore Cusamano and Dr. Steven Fiorino, for offering their time and assistance in this research.

I would also like to thank the United States Air Force and the Air Force Institute of Technology, it has been an absolute pleasure to work with such professional hosts, and I am grateful for their outstanding hospitality. I would also like to thank the Royal Australian Air Force for offering me this amazing opportunity and for their continual support throughout this assignment.

Finally, I would like to offer my thanks to my American colleagues who have continually assisted me during my endeavors, and also to my family, who have been most supportive while I've been so far from home, and who are largely responsible for any success I may achieve.

Russell McGuigan

# Table of Contents

# List of Figures

# List of Tables

x

# List of Abbreviations

EFFECT OF COUDÉ PUPIL ROTATION ON SODIUM LASER BEACON

PERSPECTIVE ELONGATION

## I.  Introduction

Adaptive Optics (AO) is a technique used to measure and improve image quality that has been distorted by optical aberrations. It is primarily used in astronomy, where the atmosphere is the cause of aberrations, and also in retinal imaging. A natural star can often be used as a reference to measure an atmospheric effect on an incoming wavefront, but may not be available in the region of interest. To compensate for this, the sodium laser guide star was developed for the Starfire Optical Range (SOR). The laser beacon produces a light source by resonating sodium atoms in the upper atmosphere, and has the advantage of being capable of being moved over any sky region of interest.

The Starfire Optical Range also operates a telescope that utilizes a Coudé path. A Coudé path uses multiple mirrors to reflect the incoming light in such a way that the optical path beyond these mirrors remains fixed in one direction, regardless of telescope orientation. Without using a Coudé path, most AO components are physically attached to the telescope, severely limiting the allowable size and complexity of optical components. A Coudé path allows equipment to be physically separated from the telescope, enabling greater flexibility in the design of downstream optics. One unfortunate effect of using a Coudé path is the rotation of the optical image as the telescope varies in azimuth or elevation. In many scenarios, this image rotation is of little concern, and can be corrected using post-processing. If used in conjunction with a side-launched laser beacon, however, asymmetries in the reference source can

degrade AO system performance.

## 1.1 Problem Statement and Hypothesis

The Starfire Optical Range operates a 3.5m telescope on a Coudé path with a sodium beacon reference for its AO system. This combination produces the unique effect of both elongating the reference source, and also rotating its relative location to the sensor. The goal of this research is to model the behavior of Shack-Hartmann Wavefront Sensor (SHWFS) performance with an AO system using a telescope with a Coudé path and a side-launched sodium Laser Guide Star (LGS). Specifically, the objectives include:

- determine the extent of Coudé rotation in a typical engagement scenario,

- model a sodium laser beacon and its elongation effects for each subaperture within a typical AO system,

- determine the effect of beacon elongation and Coudé rotation on sensor centroid measurements, and the magnitude of the resulting error after reconstructing of the original wavefront,

- test out a novel means of compensating for beacon elongation measurement errors, and

- maintain robustness in modeling the scenario, to allow changes to the engagement scenario and system configuration with minimal changes to source code.

## 1.2 Thesis Overview

Chapter II provides the background information required to develop and understand the model of this particular AO system along with the most relevant related

literature. Specifically, it details the cause and effect of Coudé rotation and perspective elongation, in addition to the basics of AO, wavefront measurement and reconstruction. Chapter III details the development of the computer model and the mathematical principals used to characterize the scenario.

Chapter IV presents the results that are produced by the computer model, providing comparisons between the current system configuration and the improvement that could be achieved through considering the effect of Coudé rotation and perspective elongation during sensor calibration.

Finally, Ch. V draws conclusions from the results presented in Ch. IV, and summarizes the key outcomes. It also suggests how to improve the current system, and outlines areas that would benefit from additional research in this area.

# II.  Background

This chapter introduces the concepts of atmospheric turbulence and its effect on the propagation of light. Adaptive optics (AO) systems are discussed as a method to measure and compensate for turbulence, and sodium laser guide stars in particular are discussed. Finally, Coudé rotation is described to enable a greater understanding of the specific issues affecting the sponsor of this work. Current literature relating to laser guide star perspective elongation is also reviewed.

## 2.1    Adaptive Optics

Light that has been transmitted through a turbulent medium can be corrected by an AO system and returned to its original form. An AO system typically consists of a Wavefront Sensor (WFS) that measures the turbulence affecting the incident light, a Fast Steering Mirror (FSM) that corrects low-order aberrations, a Deformable Mirror (DM) capable of correcting higher-order aberrations, and a controller that commands the mirrors based on WFS measurements. The primary focus of this research is the WFS, and in particular a proposed calibration technique that is designed to improve the accuracy of WFS measurements. The application is for compensating atmospheric imaging systems, so this chapter begins with a review of optical turbulence.

### 2.1.1    Atmospheric Turbulence.

The atmosphere is not a uniform medium. Localized inhomogeneities in the atmosphere cause differences in temperature, pressure and consequently index of refraction. These localized inhomogeneities are called eddies, and are defined as the volume over which the refractive index remains relatively constant. The size of these eddies can vary, but the minimum and maximum size of an eddy is defined by the inner and

4
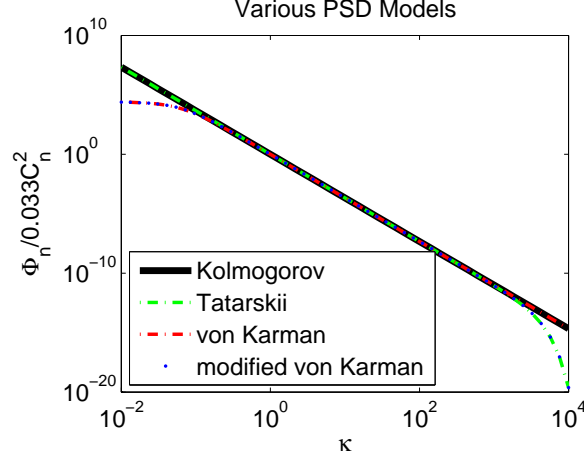
**Figure 1. Various power spectral density models.**

outer scales, $l_0$ and $L_0$, respectively. Kolmogorov characterized the Power Spectral Density (PSD) of atmospheric turbulence $\Phi$ as a function of wavenumber $\kappa$ (measured in [rad/m]) by[1]

$$\Phi(\kappa) = 0.033 C_n^2 \kappa^{-11/3}, \tag{1}$$

where $C_n^2$ is the structure constant of the variation of the refractive index in the atmosphere and effectively describes the strength of the turbulence. Equation (1) holds when $1/\kappa$ is within the inner and outer scales, or alternatively,

$$\frac{1}{L_0} \ll \kappa \ll \frac{1}{l_0}. \tag{2}$$

Wavenumbers that meet this condition are said to be within the inertial subrange of the turbulence. In Kolmogorov turbulence, the inner and outer scales are set to 0 and infinity, respectively. These values are not physically realistic, and more realistic PSD models have been developed to account for this, including the Tatarskii, von Kármán and modified von Kármán spectra[20]. These models contain additional factors accounting for inner and outer scale that are responsible for the low-frequency roll off and the high frequency cut-off, as shown in Fig. 1.
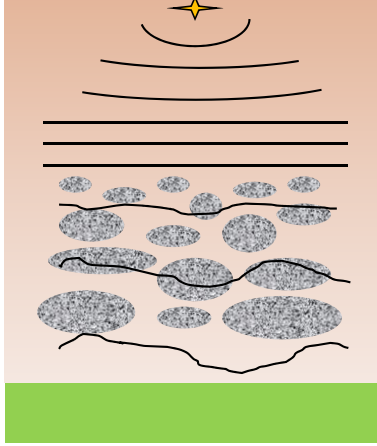
**Figure 2. The effect of eddies on an incoming wavefront.**

For light that propagates through turbulence, the different indices of refraction within various eddies cause the light to travel at different speeds. Figure 2 illustrates this by showing various wavefronts of light as it is transmitted from a star to earth. Although a star emits light spherically, it is approximately planar by the time it reaches the atmosphere of earth. As it passes through the atmosphere, the plane wave passes through eddies with varying refractive indices, causing the light to refract differently at different locations. By the time it reaches a ground-based telescope, the wavefront is no longer planar, but aberrated.

Detailed analysis of weak turbulence effects on wave propagation uses the Rytov method[1]. This method essentially solves Maxwell's equations with perturbation theory. The statistics of the perturbations are governed by Kolmogorov theory, and solutions are obtained for the turbulence-degraded field's mutual coherence function and similar quantities. The details are not presented here, just the key resulting turbulence parameters.

An aberrated wavefront can be divided into segments that are roughly spatially coherent, and this scale scale size indicates the magnitude of the turbulent phase fluctuations. The length of this segment is known as Fried's parameter, $r_0$. In the

case of an initially planar wavefront, a more formal definition for $r_0$ is[9]

$$r_0 \triangleq 0.185 \left[ \frac{\overline{\lambda}^2}{\int_0^z C_n^2(\xi) d\xi} \right]^{3/5}, \tag{3}$$

where $\overline{\lambda}$ is the mean wavelength of the incoming light and $\int_0^z d\xi$ is the integral of the path though which the light is propagating. A small $r_0$ indicates a small region of spatial coherence, and therefore large phase fluctuations. Conversely, a large $r_0$ indicates weaker phase fluctuations. For light at 500nm propagating vertically, typical values of $r_0$ range from 5-10cm.

In addition to eddies causing spatial variations in the refractive index of the atmosphere, they do not remain stationary, and hence cause temporal temporal fluctuations as well. One parameter that is commonly used to determine the rate of temporal fluctuations is the Greenwood frequency, $f_G$. Typical values of $f_G$ are of the order of 10-100Hz[1]. A formal definition is not provided here because the dynamic aspect of turbulence is not considered in this research.

### 2.1.2 Wavefront Measurement.

An aberrated wavefront can be measured by a wavefront sensor (WFS), which is required to compensate for the effects of atmospheric turbulence. One common WFS is the Shack-Hartmann (SH) WFS. The SHWFS comprises of an array of lenslets of size on the order of $r_0$. This ensures that the light incident on each lenslet is roughly spatially coherent, and can therefore be represented as a plane wave. As the plane wave passes through the lens, it is focused to a sensor in the focal plane behind it. Figure 3 depicts a lens focusing light onto a detector, and represents one lenslet within a SHWFS.

The light is not be imaged to a perfect point, as predicted by geometric optics,
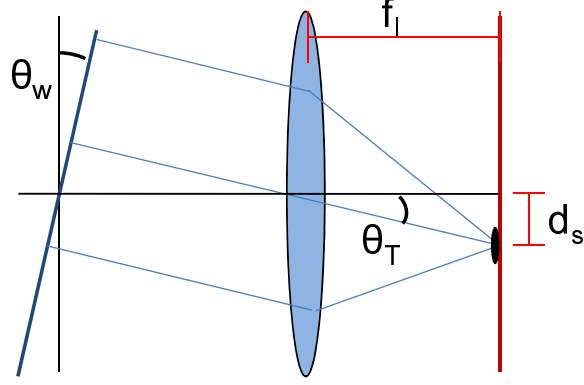
**Figure 3. The effect of a lenslet on an incoming wavefront.**

but instead is affected by the finite dimensions of the lenslet. The resulting diffraction limited spot is the Fraunhofer diffraction pattern of the lenslet, as described by Ref. [10]

$$h(u, v) = \frac{A}{\lambda z_i} \iint_{-\infty}^{\infty} P(x, y) \exp\left\{-j\frac{2\pi}{\lambda z_i}(ux + vy)\right\} dx dy, \tag{4}$$

where $A$ is the amplitude of the incident field, $\lambda$ is the wavelength of the incident light, $z_i$ is the propagation distance and $P(x, y)$ is the pupil function. For a square lenslet, Eq. (4) simplifies to

$$h(u, v) = \frac{A}{\lambda z_i} \iint_{-d/2}^{d/2} \exp\left\{-j\frac{2\pi}{\lambda z_i}(ux + vy)\right\} dx dy, \tag{5}$$

$$= \frac{Ad^2}{\lambda z_i} sinc(d\,u) sinc(d\,v), \tag{6}$$

where $d$ is the width of the lenslet.

Equation (6) describes the coherent impulse response of the system, which can be used to determine the Point Spread Function (PSF) of the system, $\mathfrak{H}(u, v) = |h(u, v)|^2$. The PSF is quite useful in incoherent imaging systems because it can be used to determine the image of any input, not just a point source. For other inputs, the diffraction image $I_i(u, v)$ is simply a convolution of the geometrically predicted image,
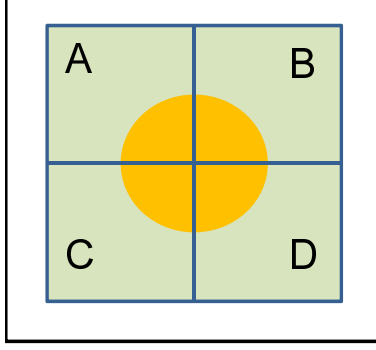
**Figure 4. Quad cell detector.**

$I_g(u, v)$ and the PSF,

$$I_i(u, v) = I_g(u, v) \circledast \mathfrak{H}(u, v). \tag{7}$$

The light focussed by a Shack-Hartmann lenslet is measured by an array of pixels at the focal plane of the lenslet. Figure 4 depicts the simplest detector, a quad cell detector consisting of a 2×2 pixel array. The individual detector pixels are referenced according to their vertical and horizontal location relative to the center of the detector. Because the imaged spot typically spans multiple pixels, the location of its center can be determined from the relative number of photons measured at each pixel. The $x$ and $y$ centroids, $x_c$ and $y_c$, can be computed by the weighted centroid calculation

$$
\begin{aligned}
x_c &= \frac{\sum_{i,j} x_{i,j} I_{i,j}}{\sum_{i,j} I_{i,j}}, \\
y_c &= \frac{\sum_{i,j} y_{i,j} I_{i,j}}{\sum_{i,j} I_{i,j}},
\end{aligned}
\tag{8}
$$

where $x_{i,j}$ and $y_{i,j}$ are the numeric indices of each pixel, indicating their location with respect to the center of the detector, and $I_{i,j}$ is the measured intensity in the $i, j$

pixel. For the quad cell detector depicted in Fig. 4, this simplifies to

$$
\begin{aligned}
x_c &= \frac{I_B + I_D - (I_A + I_C)}{I_A + I_B + I_C + I_D}, \\
y_c &= \frac{I_A + I_B - (I_C + I_D)}{I_A + I_B + I_C + I_D},
\end{aligned}
\tag{9}
$$

where $I_{A,B,C,D}$ represents the measured irradiance in pixels A,B,C and D.

For a plane wave perpendicular to the optical axis, the image is formed on the optical axis. For plane waves oblique to the optical axis, however, the image is focused to a point that is laterally displaced from the optical axis, as illustrated in Fig. 3. Although Fig. 3 shows only a one dimensional cross section of the light being imaged by the lens, the light is actually displaced in both the horizontal and vertical directions, depending on the $x$ and $y$ slopes of the incident plane wave. In a SHWFS, a detector is placed at the focal length of the lenslet and measures the intensity of the light in each pixel of the detector.

From these centroid measurements, the original $x$ and $y$ slopes of the incident wavefronts can be determined using the geometry featured in Fig. 3. Assuming the paraxial (small angle) approximation such that

$$
\sin(\theta) \approx \theta,
\tag{10}
$$

the slope of the incident wavefront, $\theta_W$, can be found from simply the lens focal length, $f_l$ and the spot displacement, $d_s$ shown in the Fig. 3. Using trigonometry,

$$
\sin(\theta_T) = \frac{d_s}{f_l} \approx \theta_T,
\tag{11}
$$

and through similar triangles,

$$
\theta_W = \theta_T,
\tag{12}
$$
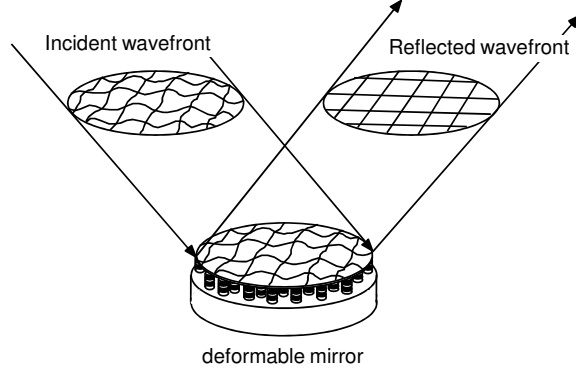
**Figure 5. Deformable mirror correcting the aberrations of an incident wavefront.**

such that

$$\theta_W \approx \frac{d_s}{f_l}. \tag{13}$$

Since the displacement of the spot is therefore determined by the slope of the incident wavefront, the centroid theoretically measure the intensity-weighted phase gradient. The measured $x$ and $y$ centroids are used to find the $x$ and $y$ slopes, $S_x$ and $S_y$. From Eq. (13),

$$\begin{aligned} S_x &\approx \frac{x_c}{f_l}, \\ S_y &\approx \frac{y_c}{f_l}. \end{aligned} \tag{14}$$

### 2.1.3 Wavefront Reconstruction.

The measured slopes from a wavefront sensor provide enough information to reconstruct the shape of the incident wavefront. Since the reconstructed wavefront is the phase of a wavefront that was originally planar, it also represents the Optical Path Difference (OPD) of the wavefront for different points across the entrance pupil. A segmented or deformable mirror can be applied to the light to compensate the OPD across the wavefront. The resulting 'corrected' image is much less aberrated, as illustrated in Fig. 5.
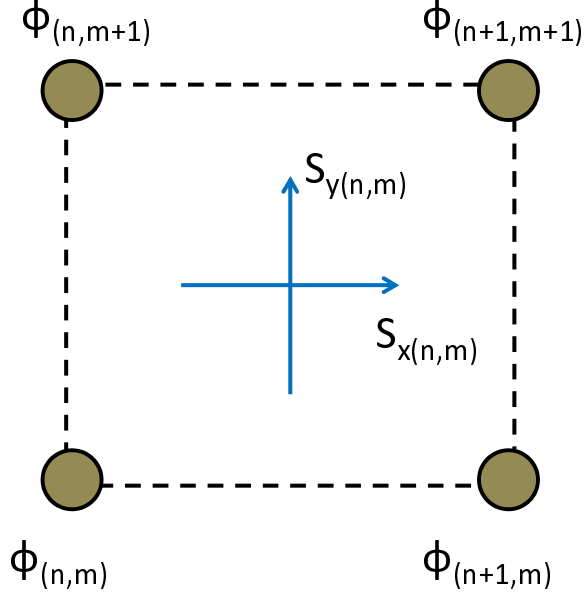
**Figure 6. The Fried geometry, as defined by the location of actuators with respect to sensor measurements.**

The location at which DM actuators are placed with respect to the SHWFS subapertures is called the system geometry. The 'Fried geometry' is defined by actuators placed at the corners of a subaperture, rather than directly over the center, where the slope measurements are made. This is illustrated in Fig. 6. In this figure, the $n, m$ subaperture is shown, with $x$ and $y$ slopes $S_x$ and $S_y$, and reconstructed phase measurements $\phi_{n,m}$ that are to be applied to the DM.

The relationship between slope measurements and reconstructed phase can be described using linear algebra, where

$$
\begin{aligned}
S_{x(n,m)} &= \frac{1}{2}\left(\phi_{n+1,m} - \phi_{n,m}\right) + \frac{1}{2}\left(\phi_{n+1,m+1} - \phi_{n,m+1}\right) \\
S_{y(n,m)} &= \frac{1}{2}\left(\phi_{n,m+1} - \phi_{n,m}\right) + \frac{1}{2}\left(\phi_{n+1,m+1} - \phi_{n+1,m}\right)
\end{aligned}
\tag{15}
$$

These equations can be written in matrix-vector form, such that

$$
\mathbf{s} = \mathsf{G}\phi.
\tag{16}
$$

12

Unfortunately, $\mathsf{G}$ is not a square matrix, so the equation cannot be solved for $\phi$ using simple matrix inverse techniques. Instead, a pseudo-inverse method can be used to retrieve phase values according to[11].

$$
\begin{aligned}
\phi &= \mathsf{G}^{+}\mathbf{s} \\
\phi &= \left(\mathsf{G}^{T}\mathsf{G}\right)^{-1}\mathsf{G}^{T}\mathbf{s} \\
\phi &= \mathsf{H}\mathbf{s},
\end{aligned}
\tag{17}
$$

where $\mathsf{H}$ is the reconstructor matrix.

Typically, approximately 87% of the phase variance caused by atmospheric turbulence can be represented by tilt[11], and can be corrected using a rigid mirror. This tilt is removed by a FSM, which greatly reduces the requirements placed on the DM. Additionally, it can typically be updated much faster than the DM, using basic tilt measurements [such as Eq. (9)] directly from a tracking camera, rather than using data from the WFS. A diagram of a standard AO system using all these components is shown in Fig. 7.

## 2.2 Laser beacons

The SHWFS described above requires a reference source to measure the effects of the atmosphere on a known wavefront. Traditionally, stars have been used as reference sources because their distance provides an almost planar wave by the time the light reaches Earth, despite originally being emitted spherically. This is illustrated in Fig. 8.

Unfortunately, natural guide stars suffer from two major drawbacks. Firstly, stars produce a relatively small amount of light to be used as a reference source, making the measurement more susceptible to noise. More importantly, a viable star may not be
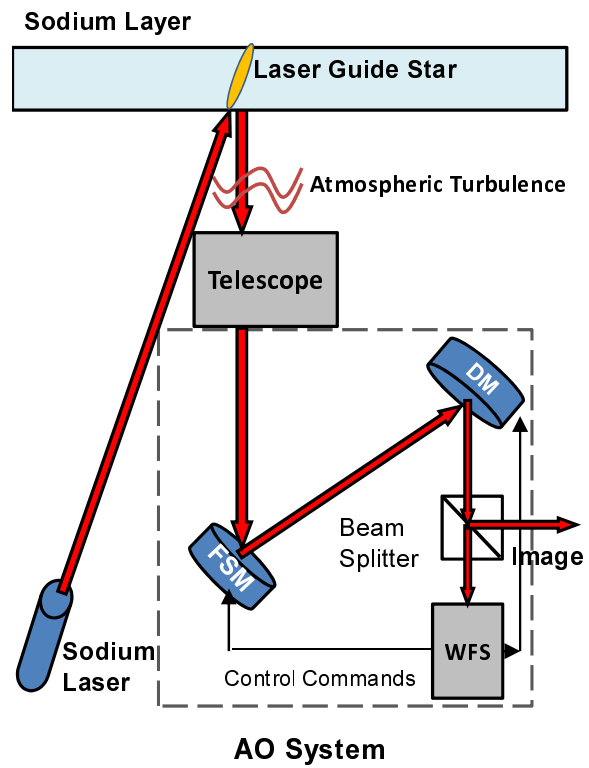
Figure 7. Adaptive Optics system.
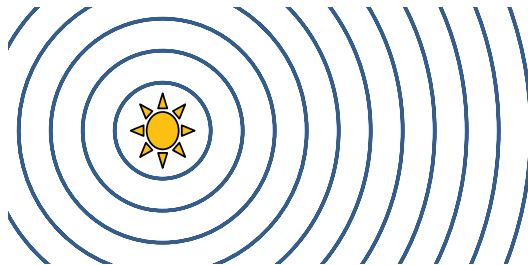


Figure 8. Spherical light waves emitted from a star appearing more planar as they propagate.

available in the region of interest, especially when moving targets are considered. For these reasons, artificial (laser) guide stars are becoming more common for adaptive optics uses.

There are two common types of LGS's, Rayleigh and sodium. Rayleigh beacons rely on Rayleigh scattering from air molecules at low altitudes (approx. 20km)[19]. These beacons can be produced for lasers of varying wavelengths, allowing relatively cheap production of high power guide stars. Unfortunately, while the majority of atmospheric turbulence occurs at lower altitudes, the cone of light measured from Rayleigh beacons does not include the majority of the atmosphere. Alternatively, sodium LGS's use resonant scattering from sodium atoms at mesospheric altitudes, much higher in the atmosphere. The light from sodium LGS's is therefore affected by a much greater volume of the atmosphere, and they provide a much more realistic representation of the effect of the total atmosphere. This is known as the cone effect, and is illustrated in Fig. 9.

One disadvantage of sodium LGS use is the requirement for a specific wavelength laser. Figure 10 shows both Rayleigh and Sodium layer scattering from a sodium laser. The much longer streak is the Rayleigh beacon, caused by low-altitude Rayleigh scattering. The much smaller spot in the upper right of the image (and inset) is the sodium guide star.

### 2.2.1 Sodium Layer.

In the upper atmosphere at an altitude of approximately 90km, there is a layer of sodium atoms at a relatively high concentration[19]. While the origin of these atoms is not certain, research[16] suggests that it may be caused by meteorites boiling off sodium as they pass through the atmosphere. The exact height and depth of this layer varies with many factors, including time and location, but the literature commonly
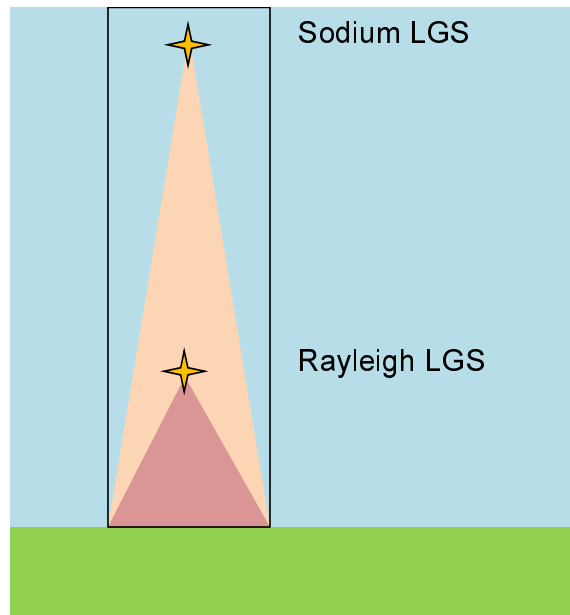
**Figure 9.** The cone effect. Due to the higher altitude of the Sodium LGS, a greater volume of the atmosphere affects the LGS, providing a more accurate reference beacon.
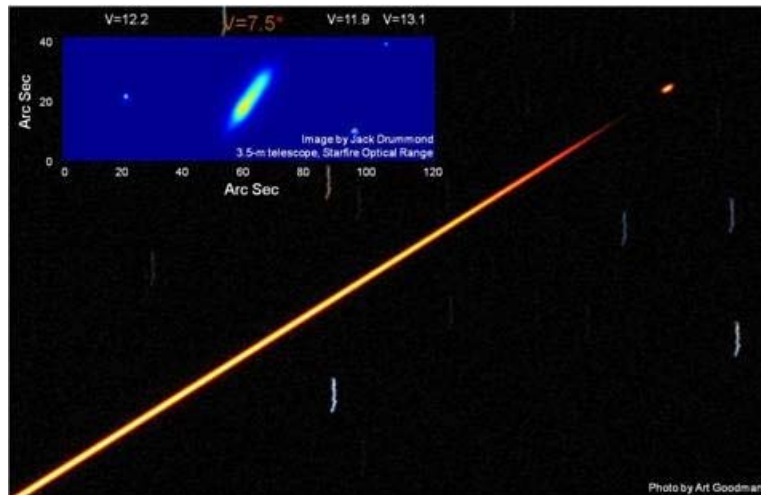


**Figure 10.** Sodium laser guide star showing Rayleigh scattering and sodium layer Resonance. Photo by Art Goodman and inset by Jack Drummond.

places the layer between the altitudes of approximately 85km–95km[3, 19] at zenith. The concentration of sodium atoms within the layer typically follows a Gaussian distribution as a function of altitude[16].

### 2.2.2 Sodium Laser.

A laser operating at the 589.2nm sodium wavelength can be created by using a Sum-Frequency Generation (SFG) technique. In this technique, two Nd:YAG lasers, one operating at 1064 nm and another at 1319 nm can be combined to produce a laser of wavelength 589 nm[14]. SOR has previously demonstrated laser output levels at the sodium wavelength of approximately 50 W[8].

### 2.2.3 Laser Guide Star Perspective Elongation.

One of the issues affecting the performance of LGS systems is perspective elongation. This is caused by the finite depth of the sodium layer and laser beam, which interact to form a 'column' of light in the upper atmosphere. When viewed directly below the column, the scattering spot appears circular, similar to how a star might appear. When viewed off-axis, however, the full height of the column becomes visible, and the spot becomes less circular and more elliptical in appearance. The further off-axis, the greater the elongation of the imaged spot. This effect can be witnessed in Fig. 11.

This issue is particularly important to consider when using a SHWFS. Centroid measurements become less accurate when modeled with an ideal spot and not the more realistic elliptical shape. The geometric details are shown in Figs. 13-15 and described in Sec. 3.1.3. These measurements affect the wavefront slope calculations, and consequently the reconstructed phase of the wavefront[21].
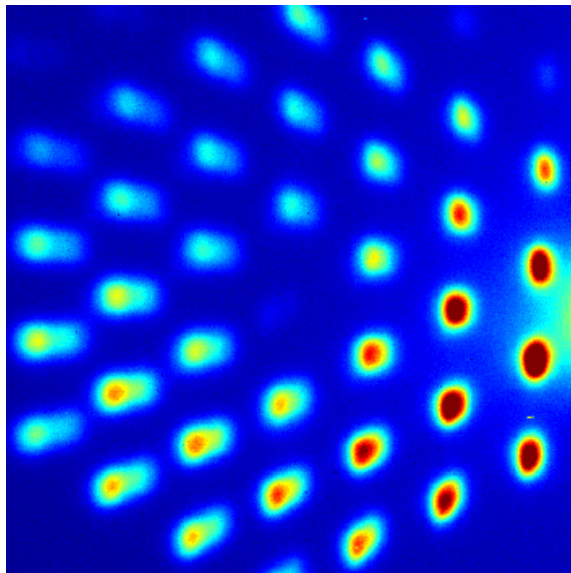
**Figure 11. Laser beacon elongation from measurements taken at the Keck observatory in Hawaii. In this image, the laser is launched from the right side of the sensor.[26].**

## 2.3   Coudé Rotation

Unlike many telescopes, telescopes that use a Coudé path are designed to provide a fixed optical axis regardless of telescope elevation and azimuth. Unfortunately, this causes the optical image to rotate as the telescope changes its orientation. A de-rotation system can be used to compensate for this effect and therefore maintain a pupil and image orientation that remains fixed, but the additional components reduce the optical throughput to the wavefront sensor[17]. Omitting the de-rotator creates additional complications when using laser beacons, due to the effects of laser beacon elongation, as each subaperture spot shape is different, as shown in Fig. 11. When the telescope moves, the pupil and laser beacon launch position rotate relative to the wavefront sensor, so these dynamically change shape.

From Ref. [13], the rotation angle from a Coudé telescope is

$$\theta_{Coude} = -\theta_{Gregory} + \theta_{el} - \theta_{az} + C \tag{18}$$

18

where $\theta_{el}$ is the telescope elevation angle, $\theta_{az}$ is the telescope azimuth angle, $C$ is a constant that describes the initial relative rotation of sensors, and $\theta_{Gregory}$ is the orientation of the object at Gregorian focus. For a stationary object such as a laser beacon, there is no rotational component at the Gregorian focus, such that $\theta_{Gregory} = 0$. From the perspective of a fixed detector, the relative angle of the laser beacon with respect to the sensor is simply the negative of the Coudé rotation of the exit pupil with respect to a fixed telescope, so that

$$
\begin{aligned}
\theta_{beac} &= -\theta_{Coude} \\
\theta_{beac} &= \theta_{az} - \theta_{el} - C.
\end{aligned}
\tag{19}
$$

Equation (19) shows that altering the elevation or azimuth of the telescope rotates the relative location of the laser beacon, which correspondingly affects the elongation of LGS spots on individual detectors as the telescope moves.

## 2.4 Starfire Optical Range

The Starfire Optical Range is located at the Kirtland Air Force Base (AFB) in Albuquerque, New Mexico. It is a laboratory facility that forms part of the Directed Energy Directorate at the Air Force Research Laboratory (AFRL). SOR houses a handful of telescopes capable of tracking earth-orbiting satellites[28]. The most notable telescope is 3.5m in diameter and is shown with its sodium laser beacon in Fig. 12. The telescope forms part of an adaptive optics system capable of compensating for the effects of atmospheric turbulence.

SOR also utilizes a side-launched sodium laser guide star, and was the first site to demonstrate closed-loop laser beacon adaptive optics[11]. Updates planned for the range in 2009 propose a SHWFS using a 32×32 array of quad cell detectors[15].

**Figure 12. 3.5m telescope at the Starfire Optical Range near Albuquerque, NM. with side lauched laser[27].**

It was predicted that the unvignetted Field of View (FOV) of the system would be approximately 0.5 mrad (100 arcsec).

## 2.5 Related Research

This section outlines the recent research relating to the compensation of laser beacon elongation effects on various systems. Several proposals that directly relate to improving measurements affected by perspective elongation are described, usually requiring expensive or complex solutions. The research described in Chapters III-V investigates the feasibility of implementing a much lower risk solution than can be implemented in software alone.

### 2.5.1 Improved Noise Model with Multiple Sensors.

Reference [2] reports the findings of a closed-loop ground-layer AO system using laser guide stars, specifically for an Extremely Large Telescope (ELT). Since the extent of beacon elongation is dependent on the ground separation between each subaperture and the laser launch position, it is a major concern for very large telescopes. Even in the preferred center-launched laser configuration, their is still a separation between

20

laser and subaperture of up to 21m for a 42m diameter ELT, compared with the maximum separation of 4.5m currently possible at SOR.

Reference [2] outlines the development of an improved noise model to account for beacon elongation in their simulations. It describes how the variance in measurement error is greatest in the axis of elongation, and how using multiple side-launched lasers with corresponding WFS's can perform almost as well as a center launched laser, if this noise model is considered. They concede that the validity of this model requires further study.

### 2.5.2    Pulsed Laser.

Reference [4] offers a unique solution to compensate for perspective elongation caused by the thickness of the sodium layer. By substituting a narrow pulsed laser in lieu of a Continuous Wave (CW) laser, they propose that the depth of the sodium layer that is illuminated by the laser at any time can be shallow enough that minimal elongation of the LGS is incurred.

Unfortunately, this solution has complications. Although the proposed pulsed lasers exist (requiring pulse lengths $<2\mu$s and enough power for adequate photon return), the WFS itself must be upgraded to work effectively with the laser. It is proposed that either the image is realigned or the WFS is moved as the illuminated volume progresses through the sodium layer. While technically possibly, this solution still requires significant work in sensor design and implementation.

### 2.5.3    Matched Filtering.

Reference [22] describes several techniques designed to improve SHWFS performance, including threshold center of gravity and weighted center of gravity. Although the techniques were proposed to analyze noise susceptibility using a symmetric LGS,

one technique may prove to be well-suited to compensating perspective elongation effects. Reference [22] proposes image correlation as a form of matched filtering to determine the actual centroid of a detected spot. The method involves correlating an ideal image with the actual detected image to determine the location of greatest similarity.

This method may severely reduce measurement errors caused by elongation, but suffers two major drawbacks. First, it would require ideal images for each subaperture and each telescope orientation, which requires more research into LGS production or experimental data. Secondly, the correlation operation is computationally intensive, and may not be a feasible solution for real-time operation with today's processing technology.

### 2.5.4   Centroid Gain Correction.

Reference [25] describes simulations designed at SOR that model the effect of perspective elongation on centroid gain measurements. The research is designed to consider a dynamic laser launch position (caused by Coudé rotation). The simulations include a Gaussian beacon model for subaperture images which is used to determine centroid gains at each subaperture by performing a calibration type operation with each image. The model shows the greatest variance in gradient measurements corresponds to the subapertures affected by the greatest elongation. The model also predicts the Strehl ratio for various scenarios, predicting increased system performance at higher elevation angles and in weaker turbulence.

The research described in Chapters III-V extends upon what is developed in Ref. [25] to consider the effect of elongation after wavefront reconstruction. The method employed to determine centroid gains in Ref. [25] is used to predict new calibration factors to improve system performance. The research in this thesis goes further to

investigate the effect of detector resolution on system performance.

# III. Methodology

This chapter outlines the methods and techniques used to achieve the objectives outlined in Chapter 1. It outlines the parameters used to represent the SOR site and the mathematical expressions that are used to model the system geometry. Finally, the implementation of these functions into MATLAB environment is described.

## 3.1 Modeling the Site

As outlined in Chapter 1, an objective of this model is to maintain robustness such that many different AO system configurations may be examined with minimal alteration of source code. Of primary concern, however, is the current configuration in operation at the Starfire Optical Range (SOR). For this reason, the SOR configuration is considered the baseline against which other setups are compared.

### 3.1.1 SOR Configuration.

Reference [15] discusses a proposed upgrade to SOR's AO system for its 3.5m telescope in 2009. The proposed upgrade is used as the baseline for modeling the AO system, and is described below:

- The primary mirror is 3.5m in diameter;

- The WFS contains an array of 32×32 subapertures; and

- Each subaperture is imaged on to a quad cell detector.

The following assumption is made about specifications not found in the literature:

- The sodium laser is launched approximately 1 m from the edge of the telescope aperture, based on pictures of the telescope and laser launch.

### 3.1.2  Turbulence Model.

The turbulence model used in this research is Kolmogorov turbulence, as discussed in Chapter 2. To simulate turbulence for a telescope viewing directly overhead, a single phase screen may be produced that mimics the phase difference from an originally planar wave that atmospheric turbulence would create[20]. To assist in simulating wave propagation, two MATLAB toolboxes were used. These are WaveProp and AOTools toolboxes, developed by the Optical Sciences Company (tOSC) [5, 6]. The included function `kolmogphzscrn` can produce a randomly drawn phase screen to model turbulence for a given $r_0$ and screen size.

To determine the required $r_0$ for the SOR site, it is necessary to determine the $C_n^2$ profile and wind model along the propagation path. The Hufnagel-Valley 5/7 (H-V$_{5/7}$) structure constant profile is commonly used, as is the Greenwood/Gaussian wind model, which depends on parameters such as wind velocity and height of the tropopause. A specific case of the Greenwood/Gaussian model is the Bufton model[1], which has been implemented in these calculations. Researchers at tOSC have indicated that these models give good agreement with atmospheric measurements made at SOR.

### 3.1.3  Sodium Layer Dimensions.

The distance to the sodium layer boundaries is a consideration that affects the extent of beacon elongation. Common values for the height of the sodium layer at zenith are around 85-95km [24, 25]. Regardless of the height chosen, the distance to the sodium layer increases as the telescope moves away from the zenith position. The geometry used to determine the distance to the sodium layer boundaries is shown in Fig 13.

The greater distance to the sodium layer boundaries at lower elevations typically
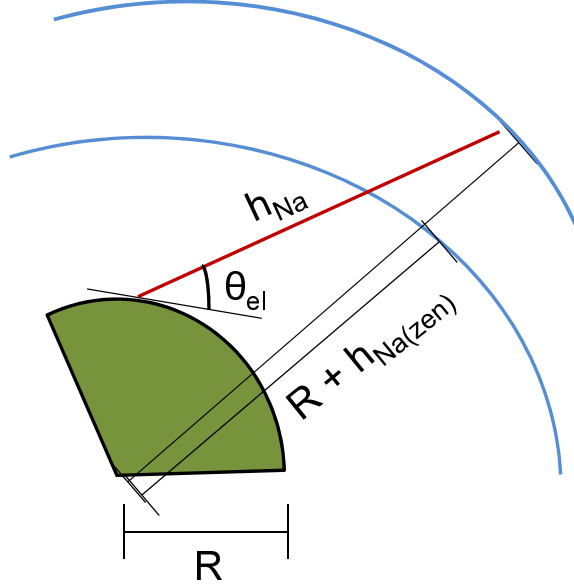
**Figure 13. Geometry showing the dependency of telescope altitude on the distance to the upper boundary of the sodium layer. The blue lines represent the upper and lower boundaries of the sodium layer surrounding a section of the earth in green. $\theta_{el}$ is the elevation angle of the telescope above the horizon.**

produce a smaller angular width of the laser beacon, corresponding to less elongation. This is despite the longer column of light produced by the laser as it travels at an angle through the layer. Using the law of cosines, the distance to the (upper or lower edge) sodium layer boundary for a given elevation angle, $\theta_{el}$, is

$$h_{Na} = R \cos\left(\frac{\pi}{2} + \theta_{el}\right) + \sqrt{(h_{zen} + R)^2 - R^2 \sin^2\left(\frac{\pi}{2} + \theta_{el}\right)}, \qquad (20)$$

where $R = 6371$ km is the average radius of the earth and $h_{zen}$ is the (upper or lower) height of the sodium layer at zenith. At zero elevation, the distances to the lower and upper boundaries of the sodium layer are therefore 104.4 and 110.4 km, respectively.

### 3.1.4 Angular Width.

For side mounted lasers, such as what is operated at SOR, the laser must be tilted to center the beacon over the telescope. This amount of tilt required affects the

26
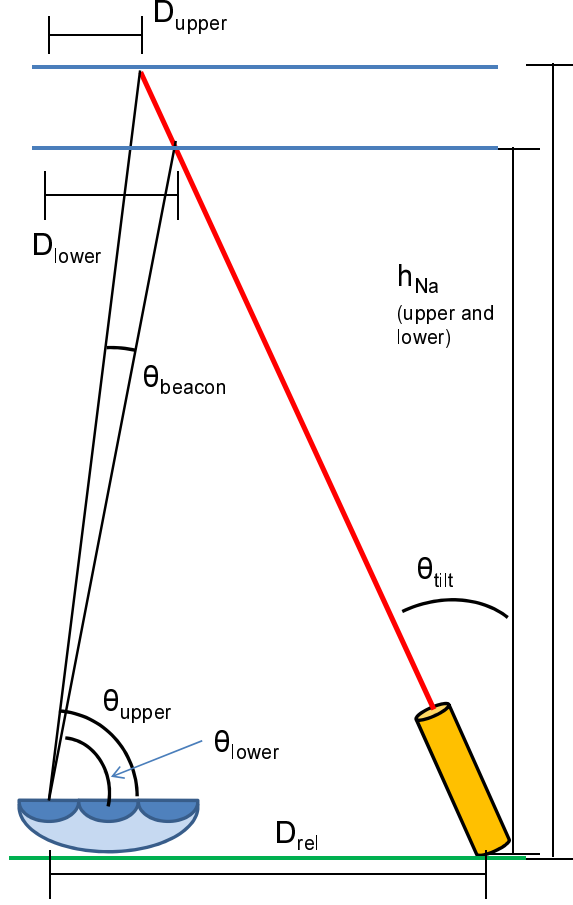
**Figure 14. Geometry showing the effect of laser tilt and distance to the sodium layer boundaries on the angular width of the imaged beacon at a particular subaperture[11].**

angular width of the beacon as viewed from a ground position. Figure 14 illustrates how the laser tilt and distance to the sodium layer boundaries are related to the angular width of the imaged beacon.

Applying trigonometry to Fig. 14, the angular width of the beacon, relative to a subaperture within the telescope is

$$
\begin{aligned}
\theta_{beacon} &= \theta_{upper} - \theta_{lower} \\
\theta_{beacon} &= \arctan\left(\frac{h_{Na\_u}}{D_{upper}}\right) - \arctan\left(\frac{h_{Na\_l}}{D_{lower}}\right),
\end{aligned}
\tag{21}
$$

where $D_{upper}$ and $D_{lower}$ are projected horizontal distances from the subaperture to
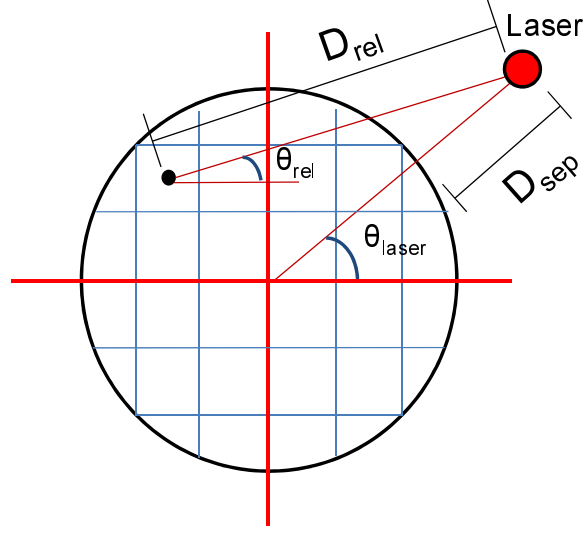
**Figure 15. Illustration of the telescope aperture showing relative distance from each subaperture to the laser beacon.**

the edge of the scattering spot, as shown in Fig. 14. $D_{upper}$ and $D_{lower}$ are given by

$$D_{upper} = D_{rel} - h_{Na\_u} \sin\left(\theta_{tilt}\right),$$

$$D_{upper} = D_{rel} - h_{Na\_u} \sin\left(\theta_{tilt}\right),$$

$D_{rel}$ is the distance from each subaperture to the laser, and $h_{Na\_u}$ and $h_{Na\_l}$ are the distances to the upper and lower boundaries of the sodium layer, respectively. $D_{rel}$ depends on the rotation of the laser beacon relative to the telescope, as calculated from Eq. (19), and the location of each subaperture within the telescope. This is illustrated in Fig. 15.

### 3.1.5  Satellite Track.

To compare the performance of various system configurations, two sample satellite paths have been analyzed. The first is the International Space Station (ISS), as it could have been viewed while it passed Albuquerque, NM on Wednesday, October

28
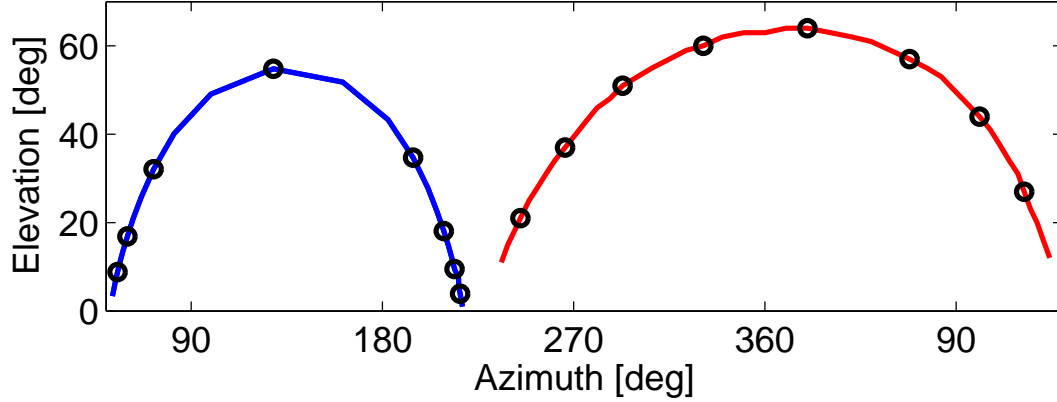
**Figure 16.** Track of two satellites as they pass over Albuquerque, NM on 20 October, 2010. The blue track is the LEO International Space Station, orbiting from right to left on these axes. The ISS passes in under 10 minutes. The red track is the MEO GPS satellite G28, orbiting from left to right and taking 7 hours to complete the pass.

20, 2010 at approximately 2130h local time. The track data is illustrated in Fig. 16, and was obtained from the NASA website[18]. The ISS maintains a Low Earth Orbit (LEO), and this particular viewing tracks almost 180° in azimuth, and reaches a maximum elevation of 54.8° above the horizon. This entire pass lasts less than 10 minutes.

The second is the path of a GPS satellite, G28, viewed from the same location between 0900h and 1600h on the same day. This satellite is orbiting in a Medium-Earth Orbit (MEO), and therefore takes much longer to complete its trajectory. This viewing tracks 258° in azimuth, and reaches a maximum elevation of 64° above the horizon. This satellite takes 7 hours to complete this pass. The track data was extracted from satellite visibility software freely available on the internet[23].

These satellites were chosen primarily due to the availability of track data and difference of orbit types. The key benefits of these orbits are their relatively high elevation angle and wide azimuthal change compared to other crossings. The greater change in telescope orientation required to view these satellites ensures that the Coudé effect is more evident than in tracks which vary less in azimuth and elevation. Eight

equally spaced points along each track are analyzed in this research.

## 3.2   Modeling the Wavefront Sensor

The preceding section described the environment being modeled, including the physical characteristics of the target, transmission path and receiving telescope. This section provides detail about how this information is applied to model the impact to the sensor.

As in a real AO system, the Shack-Hartmann sensor must be calibrated against a known source to determine the relationship between the tilt present on a wavefront to the resulting lateral displacement of the spot imaged behind each lenslet. This is typically achieved in a laboratory by using a calibration laser that acts as a point source, i.e., has no finite extent nor elongation.

Once wavefront slopes have been measured by the WFS, they are corrected according to this system calibration. The incident wavefront can then be corrected through commands sent to the DM, based on the reconstruction of these slope measurements. The research described here uses this technique as a baseline but also models more realistic reference sources based on the previous geometric discussion. It is hypothesized that these new reference sources produce more accurate calibration factors and therefore reduce errors in the reconstructed wavefront.

Finally, the reconstructed wavefront is used to quantitatively determine how perspective elongation and Coudé rotation affect the performance of wavefront measurements and allow effective comparisons between different configurations to be performed.

### 3.2.1 Subaperture Images.

Modeling the unaberrated shape that the beacon produces as viewed from the telescope is considerably complex, due to these factors:

- the laser beam is slightly diverging as it passes through the sodium layer,

- the laser beam varies in spatial intensity,

- the density of the sodium atoms within the sodium layer varies, and depends on many factors, and

- each lenslet views the beacon from a unique perspective angle, based on its location within the aperture.

Due to these factors, an accurate analytic model is very difficult to achieve. From a simply qualitative perspective, empirical data shows that the beacon appears to have an elliptical shape, such as in Fig. 11. This model therefore uses a simple two-dimensional asymmetric Gaussian intensity distribution to as a first order approximation of the beacon in each subaperture. This Gaussian function is given by

$$f(x,y) = a \exp\left[-\frac{(x-x_{offset})^2}{2c_x^2} - \frac{(y-y_{offset})^2}{2c_y^2}\right], \tag{22}$$

where $a$ is a constant, $x, y$ represent the spatial position in the subaperture with respect to the major and minor axes of the ellipse (in meters), $x, y_{offset}$ represent the lateral displacement of the spot with respect to the center of the subaperture, and $c_x, c_y$ represent the width of the spot's intensity along the major and minor axes of the ellipse.

For simpler computations, the major and minor axes are aligned to a Cartesian grid, and coordinate transformation is used to rotate the shape of each subaperture image so that the major axis is aligned with $\theta_{laser}$. The transformation used to create

the rotated grid coordinate system $(x_2, y_2)$ from the original coordinates $(x_1, y_1)$ at an angle of $\theta_{laser}$ is given by

$$
\begin{aligned}
x_2 &= x_1 \cos \theta_{laser} - y_1 \sin \theta_{laser}, \\
y_2 &= x_1 \sin \theta_{laser} + y_1 \cos \theta_{laser}.
\end{aligned}
\tag{23}
$$

This transformation allows the angular width of the minor axis to be held constant, representing the width of a non-elongated beacon. For this model, $c_y$ is kept at 0.1, representing an ellipse about 1m wide at zenith, which matches measurements presented in Ref. [25], and appears similar to actual data presented in Ref. [4].

As previously discussed, the angular width of the major axis varies according to the perspective of the laser beacon as viewed from the telescope. To produce the diffraction image present at the detector, the Gaussian function is convolved with the PSF of the Shack-Hartmann lenslet in the spatial domain. The relative widths of the PSF and the Gaussian functions therefore determine how much of an effect the elongation has on the resulting image. If the width of the beacon image is much narrower than the PSF, the elongation is somewhat masked in the convolution process. In the system that is being modeled, the beacon image ranges from roughly the same size of the PSF to about 50% larger, depending on the location of the subaperture and elevation of the telescope.

The convolution of the two functions is performed using a high-resolution grid to adequately capture the effect of the beacon shape, and the intensity of the resulting diffraction image is integrated over each pixel's area in the detector to produce photocounts. In this model, the effect of shot noise on the detected photocounts is not considered.
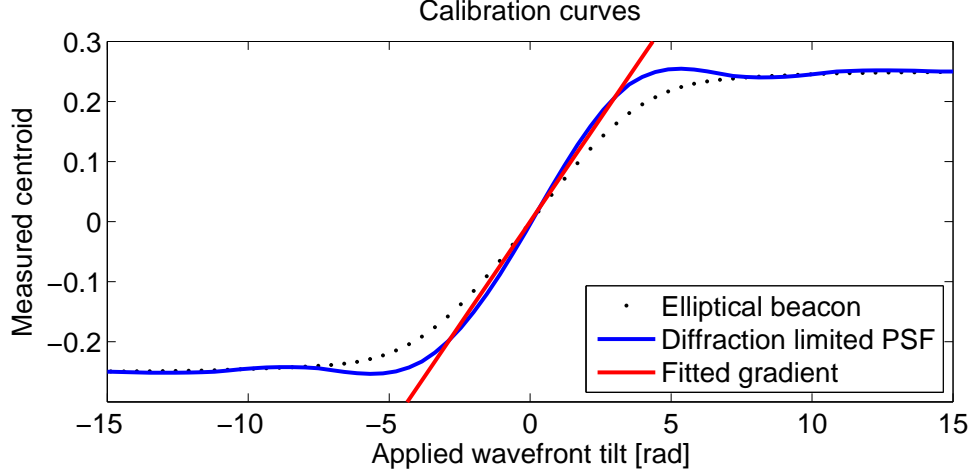
**Figure 17. Calibration curves for a quad-cell detector. The $x$ axis shows the amount of tilt (in radians of wavefront slope) applied to the imaged beacon, and the $y$ axis shows the location of the measured centroid (in units of detector width). The blue curve is achieved using the basic $sinc^2$ function, whereas the dotted black curve is from an elongated beacon on the opposite side of the telescope from the laser.**

### 3.2.2   Calibration.

The centroid calculation in Eq. (9) does not perfectly determine the center of an imaged spot, primarily due to the discrete nature of the pixels that are measuring a continuous spot. The accuracy can be improved by using more pixels within a subaperture, but a basic quad cell is commonly used, as is the case in this model.

To account for this, a calibration curve is often produced to determine the measured centroid for a given tilt. A source providing a diffraction-limited spot is applied with varying tilt. As the applied tilt is varied, the measured tilt typically follows an "S-curve". Figure 17 shows two such calibration curves, one for a point source and another for an elliptical Gaussian beacon.

Due to the fact that the curve is nonlinear, the sensor is typically designed to ensure that during normal operation in turbulence most of the local tilt on a subaperture is within the central, linear region of the curve. The slope of the curve in this region determines the conversion required between measured and applied tilt.

In this research, two cases are compared. The initial uses the traditional method of calibration, with a diffraction limited spot as the reference source. This spot is translated across the detector at fine increments, and the centroid calculation is performed at each location to determine the measured tilt and produce the calibration curve. The gradient of the linear region is determined by using MATLAB's `polyfit` function to fit a first order polynomial between two points very close to the center of the curve. The second case performs all the above steps, but uses the more realistic elongated beacon image as the reference source.

The relative size of the imaged spot and the pixels that measure it affect the gradient of the linear region of the calibration curve. It is therefore during sensor calibration that the difference between calibration with a traditional reference source and an elongated source will be highlighted, and provide the means to quantify the effect of perspective elongation on wavefront measurements.

## 3.3    Reconstruction

To reconstruct the aberrated wavefront that is represented by the phase screen described in Section 3.1.2, the local tilt across each subaperture must be calculated and applied as a lateral shift of the Gaussian function. The $x$ and $y$ gradients of the high resolution phase screen is determined using MATLAB's `gradient` function. The gradient values of the phase screen are averaged across each subaperture to determine the average wavefront gradient across each subaperture. The centroid of the shifted images, which are the intensity-weighted phase gradients, are then determined and the sensor calibration factor is applied.

Once slope measurements are obtained, the original wavefront can be reconstructed as described in Section 2.1.3. Typically, calculating the reconstruction matrix which relates the measured slopes at each subaperture to the measured wavefront at

34
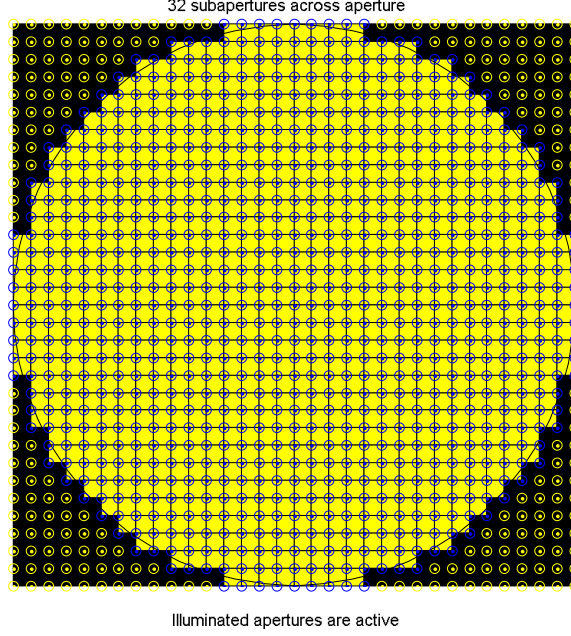
**Figure 18. WaveProp's** *subapdlg* **toolbox, used to generate reconstruction matrices for different system geometries.**

each of the DM actuators is not an easy endeavor. Fortunately, AOTools contains a tool which generates the geometry matrix and various reconstruction matrices for a user-specified AO geometry. This tool is called `subapdlg`, and it allows the user to input the number of actuators, number of subapertures, and the shape of the pupil mask. A plot of the geometry used in this research is shown in Fig. 18. This plot was generated by `subapdlg`.

Reconstruction of the incident wavefront provides enough information to determine the benefit resulting from an enhanced calibration method. The reconstructed wavefront is calculated in units of radians, representing the phase difference between two points in space. The wavefronts of the original and enhanced calibration wavefronts can be compared against a wavefront that is reconstructed from the original phase screen values to determine the wavefront error in each case. The root mean square error of the phase differences at each subaperture is calculated and the average over all active subapertures provides a metric to compare the methods.

35

# IV. Results and Analysis

This chapter presents the results that were obtained using the methods discussed in Chapter 3. The impact of telescope orientation, turbulence parameters, and detector resolution are considered to characterize the effect of beacon elongation and rotation. The primary metric used to score the performance of calibration methods was Root Mean Square (RMS) phase error between reconstructed wavefronts.

## 4.1 Rotation Effects

Equation (18) describes how to determine the amount of rotation caused by a Coudé path for a given trajectory. Using the ISS satellite track data from [18], the Coudé rotation angle at each satellite position was determined, and is displayed in Fig. 19. For this particular path, the telescope aperture rotates at 21.4 deg/minute on average, and rotates less at lower elevations where the azimuthal angle to the ISS changes much less.

## 4.2 Calibration Effects

As described in Sec. 3.2.2, the wavefront sensor requires calibration to determine the detected subaperture tilt that is caused by a known reference tilt. The typical method performs the calibration using a point source as the reference beacon, which does not consider the effects of beacon rotation and elongation. Equation (7) describes that the resulting PSF using square lenslets is a $sinc^2$ function. Figure 20 shows the result when this PSF was implemented using a side resolution of 64 grid points.

The width of the PSF is an important factor to consider. Since the literature did not describe the complete specifications of the sensor, the PSF was chosen to cover roughly half of the detector area, which appears to match empirical data provided

36
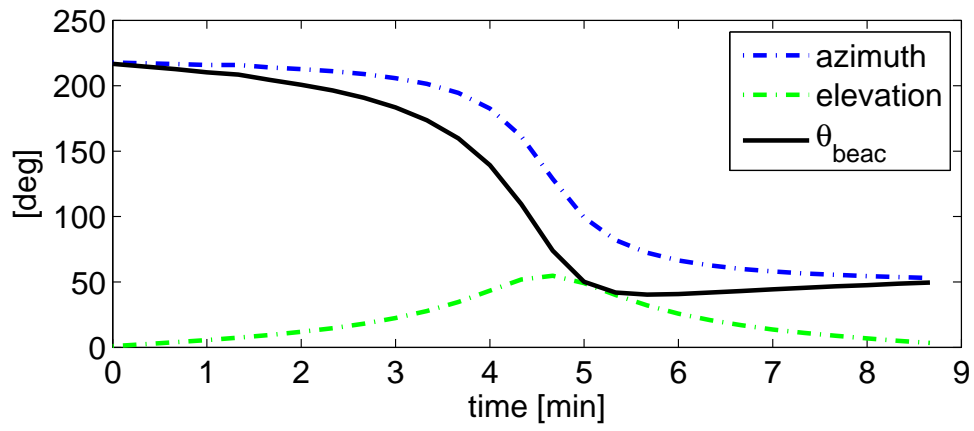
Figure 19. Coudé rotation caused by changes in target azimuth and elevation.
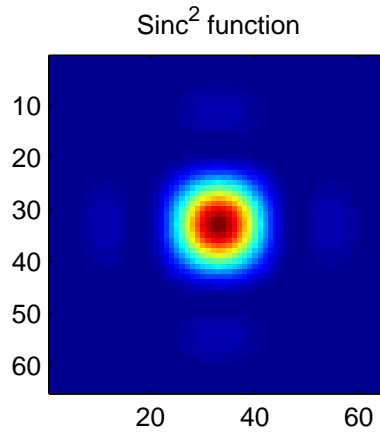


Figure 20. Diffraction limited point spread function. This axes of this image represent the width of one subaperture.

in Ref. [4]. The validity of this PSF is also checked against metrics used by tOSC to design Shack-Hartmann sensors. tOSC define a parameter $n_{lod}$, or 'number of spot half-widths per subaperture', to characterize the subaperture field of view, and defined it as

$$n_{lod} = \frac{d}{\frac{f\lambda}{d}} = \frac{d^2}{f\lambda}. \tag{24}$$

As a rule of thumb, the sensor should have between 6 and 8 $\times n_{lod}$ across each detector[7]. By setting the null-to-null width of the diffraction limited PSF in the model to 2 (in arbitrary units due to the undefined lenslet diameter $d$ and focal length $f$), the diffraction limited spot size is given by[12]

$$
\begin{aligned}
= \frac{2f\lambda}{d} &= 2, \\
\therefore \frac{f\lambda}{d} &= 1.
\end{aligned}
\tag{25}
$$

If the detector width is set to 3.5 (in the same arbitrary units), $n_{lod}$, is also equal to 3.5. This is less than the ideal case of 6-8 [7], but not impractical. Furthermore, the number of pixels, $n_{pix}$ per $\lambda/d$ is another sensor specification relating to its resolution. This value changes, depending on the detector chosen, but typically should be greater than two to resolve a spot. For a quad cell this is 1.75, and for a $4 \times 4$ detector it is 3.5. What these numbers indicate is that the PSF is not resolved or Nyquist sampled in a quad cell detector, but is for the $4 \times 4$ scenario.

Also, a PSF at this width is generally slightly larger than the geometric beacon image for subapertures near the laser launch, and noticeably smaller than the geometric beacon image at greater elongations. Figure 21 shows the minimum and maximum size of a beacon image caused by perspective elongation. These images contain the entire FOV of the subaperture, as is the case of Fig. 20, for easy comparison. The relative sizes of the beacon image and PSF determines the size and shape of the
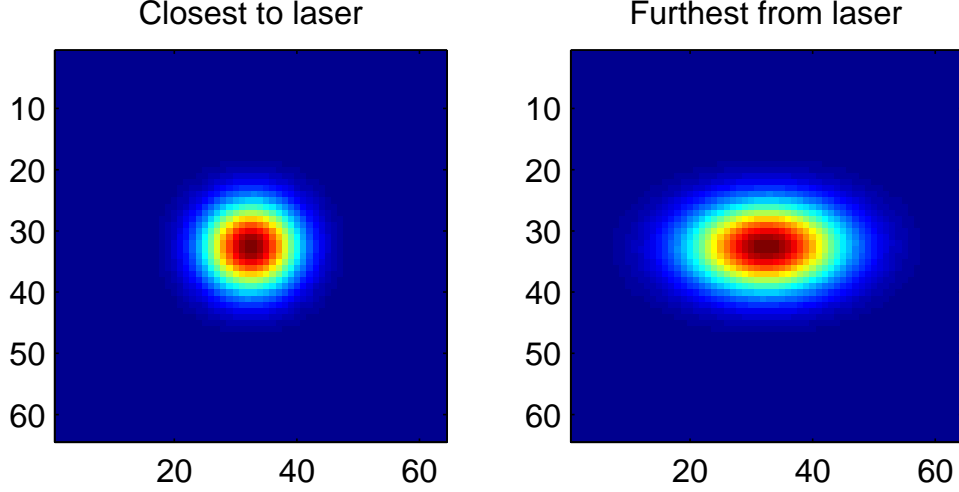
**Figure 21. Beacon images at two subapertures. The left image shows the beacon as viewed from the subaperture closest to the laser, and the right image shows beacon from the furthest subaperture. These beacon images are taken at an elevation angle of 60 degrees, and would be slightly different at other angles, as discussed in Sec. 3.1.4**

diffraction image after the convolution operation.

### 4.2.1 Standard Calibration.

In the calibration method that is typically performed, the detector is calibrated by computing the centroid of the PSF as it is translated at regular intervals, simulating the effect of local tilt. The calibration curve that is obtained for a quad cell detector is shown in Fig. 17. The $y$-axis of Fig. 17 is measured in detector width, and the $x$-axis in radians of wavefront slope, which can be easily converted to optical path difference measured in wavelengths. Note that the maximum measurable displacement for a quad cell detector is $\pm 0.25 \times d$, where $d$ is the detector width. This is the center of the furthest pixel, corresponding to the case where the entire PSF is contained within this pixel. At this tilt, the sensor is beyond its useful linear region, and the sensor is designed such that the expected magnitude of wavefront slopes do not cause this amount of tilt.

This calibration curve also determines the extent of the linear region of the detec-

tor. In Fig. 17, this corresponds to roughly 30% of the detector width. The sensor is designed such that the maximum expected local tilt rarely deflects the centroid of the PSF beyond this point. This ensures that a linear calibration factor can be used to represent the curve without too much error.

To determine the calibration factor, MATLAB®'s `polyfit` command was used to fit a line to the center region of the curve as shown in Fig. 17. Due to symmetry of the point source's image, this curve is identical for both the $x$ and $y$ directions.

### 4.2.2   Enhanced Calibration.

When considering the effects of elongation and rotation on the beacon image shape, a new reference source is required for each subaperture. This alters the calibration curve at each subaperture, since the beacon image varies depending on the relative distance and angle between the subaperture and the laser. Creating a reference source that emulates beacon elongation and rotation for laboratory use is difficult and has not currently been achieved. This research explores a low risk solution to providing these calibration values without producing a new reference source.

The slope of the line fitted to the linear region of the calibration curves (the calibration factor) for every subaperture is shown in Fig. 22. The lower calibration factors represent subapertures where the beacon has greater elongation, which generally increases the linear region of the detector. Additionally, the calibration factors for the $x$ and $y$ directions differ due to the anisotropic beacon image.

These new calibration factor predictions are the key to reducing the phase error of the reconstructed wavefront. If the gradients from a standard calibration (which does not consider beacon elongation) were displayed in a similar manner, it would remain a constant value across the detector due to symmetry of the PSF. Furthermore, the Coudé rotation at the sensor causes these calibration gradients to change with

40
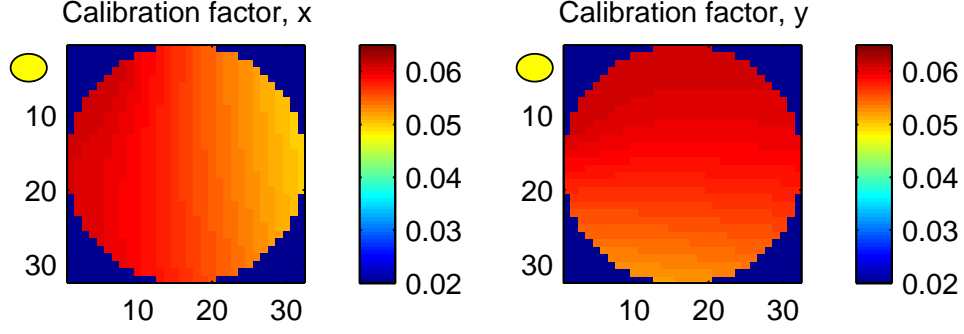
**Figure 22. Calibration factors over the entire sensor. Note the relative direction of the laser and its effect on the calibration factor across the aperture. Subapertures furthest from the laser are affected by the most elongation, lowering the gradient of the calibration curve.**

telescope orientation, preventing the use of a simple calibration method using an elongated source in one orientation.

## 4.3   Sensing Turbulence

To model the effect of turbulence, randomly drawn phase screens are generated using the AOTools function `kolmogphzscreen`, such as the phase screen shown in Fig. 23. This phase screen is continually used throughout this chapter to illustrate the benefit of the enhanced calibration method.

To generate this phase screen, 1024 grid points were used across an aperture size of 3.5m. The coherence diameter is set to 6.1cm for the standard case, and 50% and 200% of this value for comparison, based upon $r_0$ calculations for the SOR site, as described in Sec. 3.1.2. The phase screen is generated without adding any global tilt, similar to a wavefront after the majority of tilt has been removed by a fast steering mirror.

The local $x$ and $y$ wavefront gradients are then computed using MATLAB®'s `gradient` function. These gradients are subaperture-averaged to align to WFS measurements, as shown in Fig. 24. These local gradients are converted to a translation
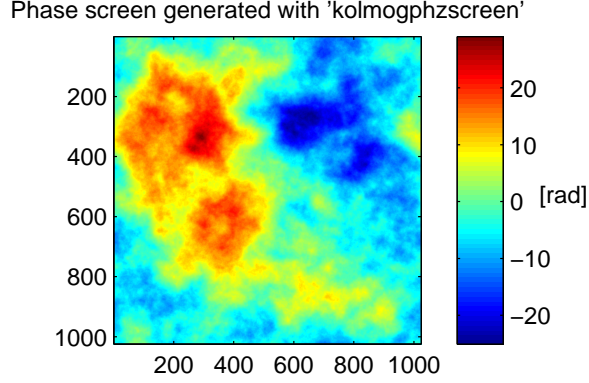
**Figure 23. Phase screen simulating the effects of turbulence on a planar wavefront.**

of the PSF at each subaperture, modeling the effect of propagation through a Shack-Hartmann lenslet to the detector. The shift is induced as the $x_{offset}$ and $y_{offset}$ variables in Eq. (22). The displacement of the turbulent Shack-Hartmann spots are then measured using the centroid algorithm over the desired number of pixels.

The wavefront slope at each subaperture is then determined by applying the centroid-dependent calibration factor to each centroid measurement. As expected, the measured slopes obtained from the standard calibration varied from the enhanced calibration.

## 4.4   Reconstruction

Finally, the measured wavefront slopes are reconstructed into phase values through Eq. (17). The reconstructor matrix, **H**, was obtained through AOTools `subapdlg` tool. Several stages of the subaperture averaging and reconstruction process are shown in Fig. 25. Although both results appear similar to the original phase measurements, taking the difference between them shows more clearly how much more accurate the enhanced calibration method is. Figure 26 shows the difference between the reconstructed and original phase. There is a fixed color scale for both images in Fig. [26], highlighting the much lower phase error produced by using the enhanced
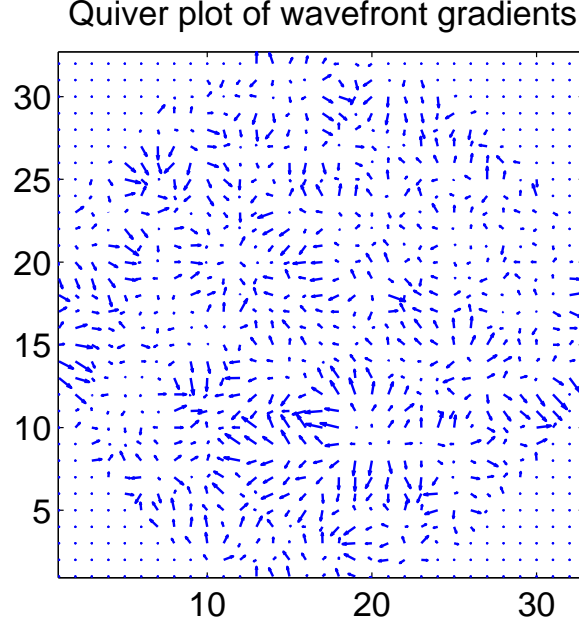
**Figure 24. Quiver plot of randomly generated wavefront slopes taken from the phase screen in Fig. 23 before any calibration factor has been applied. The magnitude of the largest slope is 8.32 radians per subaperture. These arrows also correspond to the relative displacement of Shack-Hartmann spots.**

calibration method.

## 4.5 Performance

The metric used to determine the performance of the model is the root mean square error (RMSE) between the incident and reconstructed wavefront phase. To eliminate the effect of reconstruction error, the reconstructed phases are not compared directly to the original phase screen, but instead to the reconstruction of the downsampled phase screen gradients. 50 iterations using different atmospheric phase screens were used at each telescope orientation corresponding to a satellite position, and the RMS phase error at each subaperture was averaged over each iteration to determine the final RMSE.

The number of iterations ran for each orientation of the telescope was verified by calculating the standard deviation, $\sigma_{RMSE}$, and mean, $\mu_{RMSE}$ RMS phase error
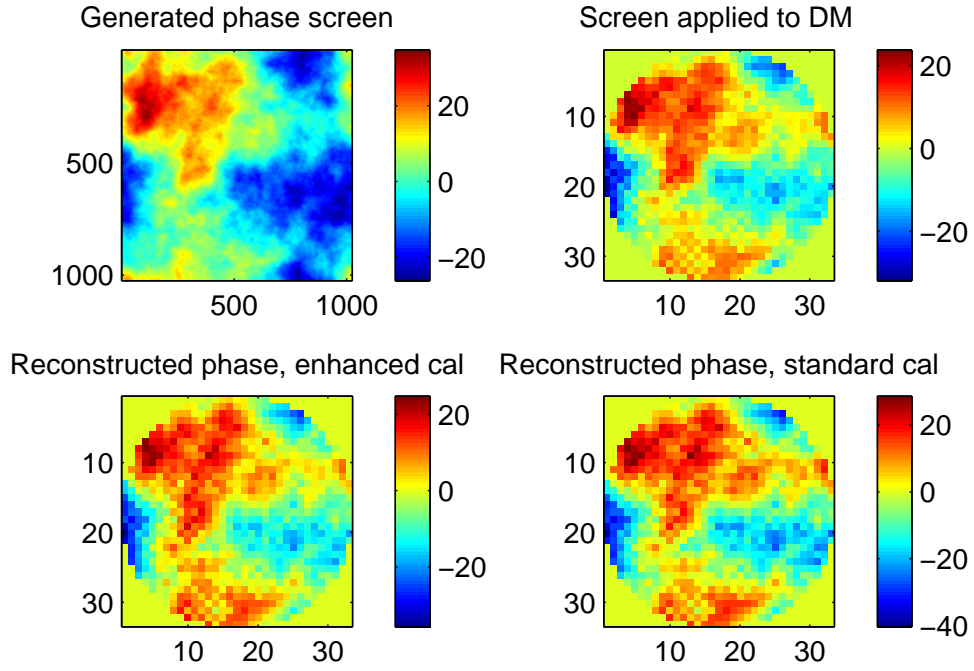
**Figure 25. Example wavefront at various stages of reconstruction. Initially, the wavefront is downsampled from a high resolution to be fitted to the DM. The difference between reconstructed phase from the different calibration techniques is only slightly evident here.**
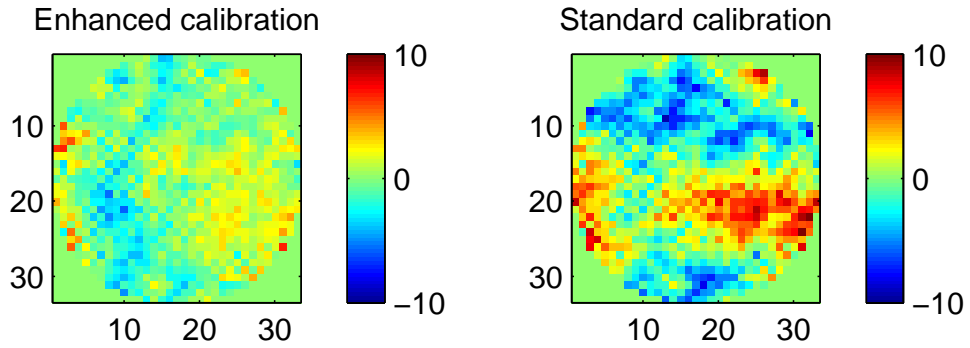


**Figure 26. Difference between reconstructed and original phase.**
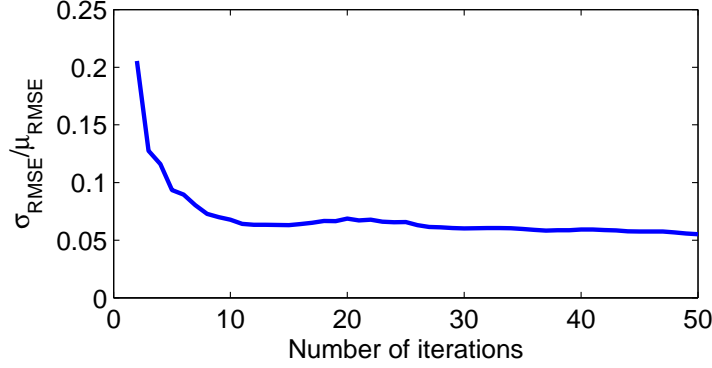
**Figure 27. Checking that enough iterations of turbulence are used in this model.**

**Table 1. Average Root Mean Square Error of reconstructed phase over ISS path.**

| $d/r_0$: | 3.59 | | 1.79 | | 0.90 | |
|---|---|---|---|---|---|---|
| detector size: | 2×2 | 4×4 | 2×2 | 4×4 | 2×2 | 4×4 |
| standard cal | 9.59 | 2.94 | 3.89 | 0.63 | 1.63 | 0.21 |
| enhanced cal | 7.17 | 2.75 | 1.98 | 0.50 | 0.29 | 0.13 |
| error reduction | 25.2% | 6.5% | 49.1% | 20.6% | 82.2% | 38.1% |

after each iteration. The results of this analysis with a quad cell detector with using standard calibration and with $r_0 = 3.05$cm are shown in Fig. 27. As a general rule, the number of iterations was deemed sufficient when the standard deviation of the data set was less than 10% of the mean. In this circumstance, 50 iterations is more than sufficient. Other configurations were tested with similar results.

The average phase RMSE across all detectors over 50 iterations of the ISS path is shown in Table 1, as a function of $r_0$ and detector resolution. As expected, the results show a decrease in RMS phase error as the $d/r_0$ value decreases, since the system is affected by weaker turbulence. Similarly, the transition from a quad cell detector to a $4 \times 4$ pixel detector reduces the RMS phase error in each case. The RMSE is reduced by 49.1% through using the enhanced calibration method, compared to 20.6% if the detector was upgraded from a quad cell to a $4 \times 4$ pixel detector. Detectors with even greater resolution were investigated, but the reduction in error was almost negligible.
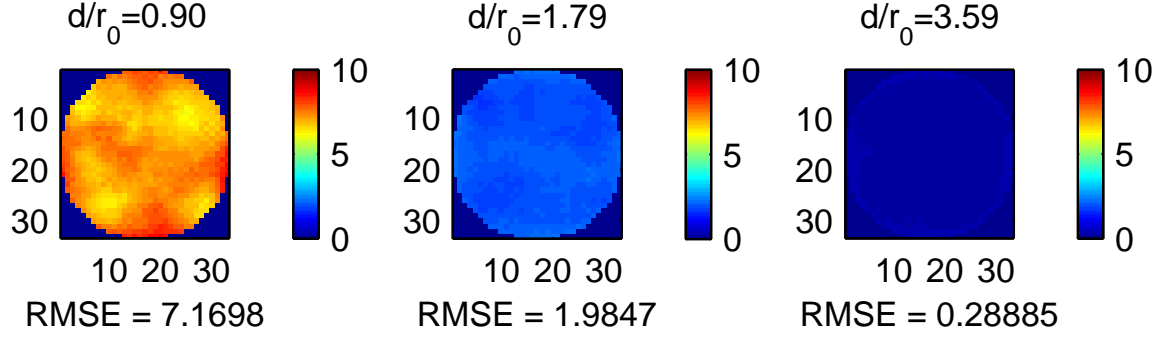
**Figure 28. Effect of turbulence on sensor measurements.**

## 4.6  Analysis

The quad cell detector with $r_0 = 6.1$cm was considered the baseline configuration against which other configurations were compared. The value of $r_0$ was first increased then later decreased by a factor of 2 to determine the effect of atmospheric turbulence strength on the results. Secondly, the detector resolution was improved, and finally, a second satellite path was used to validate results. Overall, the results show that considering elongation effects during calibration can reduce RMS wavefront error by approximately 50% for the standard operating configuration, with typically less noticeable benefits outside of this configuration. Images of the complete results are displayed in Sec. 4.7.3.

## 4.7  Atmospheric Effects

The atmospheric coherence diameter was varied to represent varying turbulence strengths to determine the effect on wavefront error. It was expected that the model would show improved performance with larger coherence diameters. The mean RMSE of the reconstructed wavefront is shown in Fig. 28.

As expected, increasing the atmospheric coherence diameter decreased RMS phase error. In the quad cell configuration, RMSE was reduced from from 7.17 rad at $d/r_0 =$
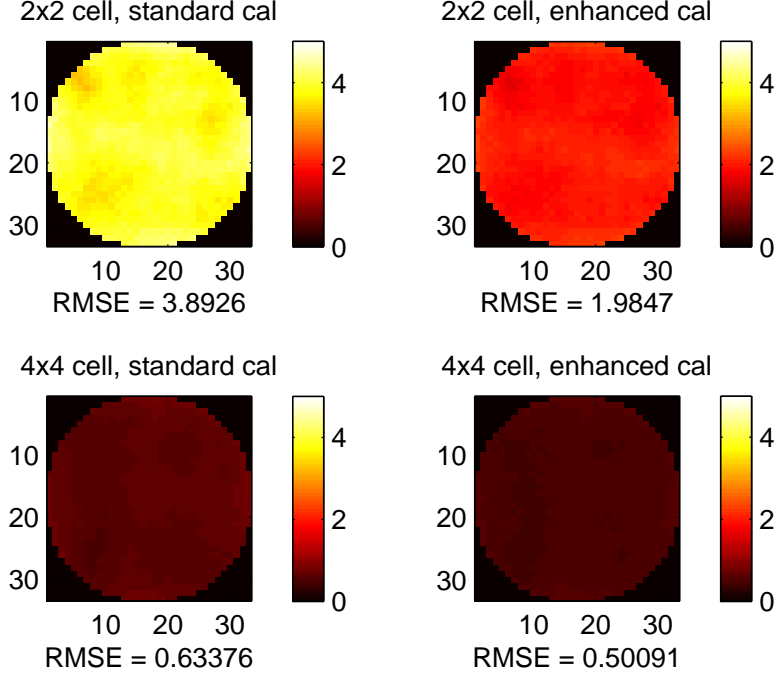
**Figure 29.** **Effect of detector resolution on sensor measurements. The left column show the effect of improved resolution without using the enhanced calibration method, while the right column shows the improvement after applying the appropriate calibration factors.**

3.59 to 0.29 rad at $d/r_0 = 0.90$. This is a positive result, confirming expectations.

### 4.7.1 Detector Resolution.

The detector was increased in resolution from a quad-cell to a $4 \times 4$ cell detector to characterize the effects of detector resolution on measurements. The improvement gained by using the enhanced calibration technique was noticeably less in this case compared to the quad cell detector, due to the extended linear region for both elongated and diffraction limited spots over 4 pixels. Detectors with resolutions greater than $4 \times 4$ pixels were briefly investigated, but showed almost negligible improvement due to a much greater linear region and much more precise centroid calculations.

**Table 2.** Average Root Mean Square Error of reconstructed phase over GPS path.

| $d/r_0$: | 3.59 | | 1.79 | | 0.90 | |
|---|---|---|---|---|---|---|
| detector size: | 2×2 | 4×4 | 2×2 | 4×4 | 2×2 | 4×4 |
| standard cal | 9.52 | 3.05 | 3.91 | 0.66 | 1.63 | 0.23 |
| enhanced cal | 7.01 | 2.83 | 1.94 | 0.51 | 0.27 | 0.14 |
| error reduction | 26.4% | 7.2% | 50.4% | 22.7% | 83.4% | 39.1% |

### 4.7.2  Trajectory Differences.

The GPS satellite orbit path showed little difference in the effect on performance of the sensor when compared to that of the ISS. This was expected, as the overall sensor performance should not be affected by changes in the Coudé rotation of the beacon. The full results of the GPS trajectory are shown in Table 2.

### 4.7.3  Complete Results.

The complete results for each turbulence strength, detector resolution and path type combination are shown in Figs. 30–33. These figures show the difference in RMSE between the typical calibration method (top) and the enhanced calibration method (bottom). The $d/r_0$ value decreases from left to right. For a 3.5m telescope with 32 subapertures across, $d = 10.94cm$. The $r_0$ value for the center plots is 6.1cm, but is 50% smaller for the left plots and 100% greater for the right. These figures show that the enhanced calibration method produces less error than the standard calibration in all scenarios, but provides the greatest benefit in the quad cell scenario.
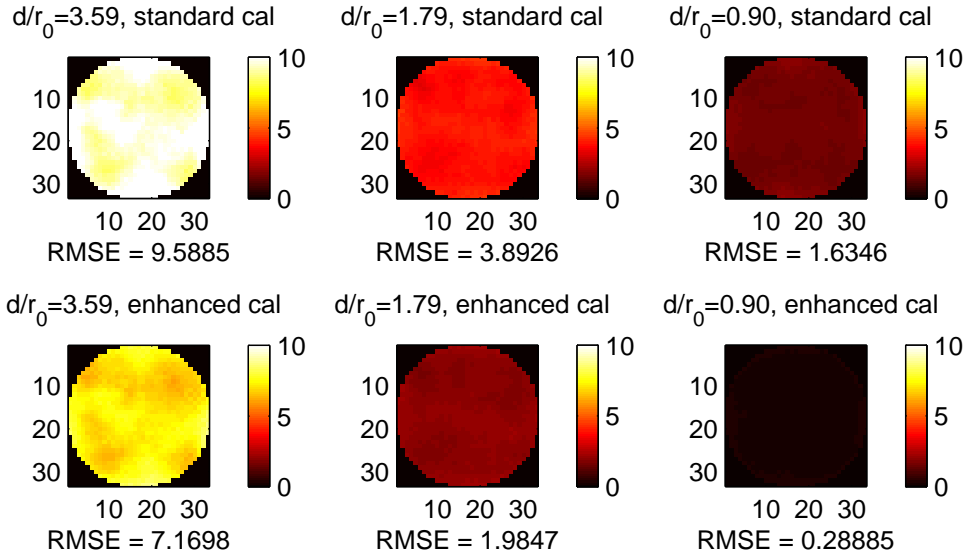
**Figure 30. Full results, ISS path, quad cell.**
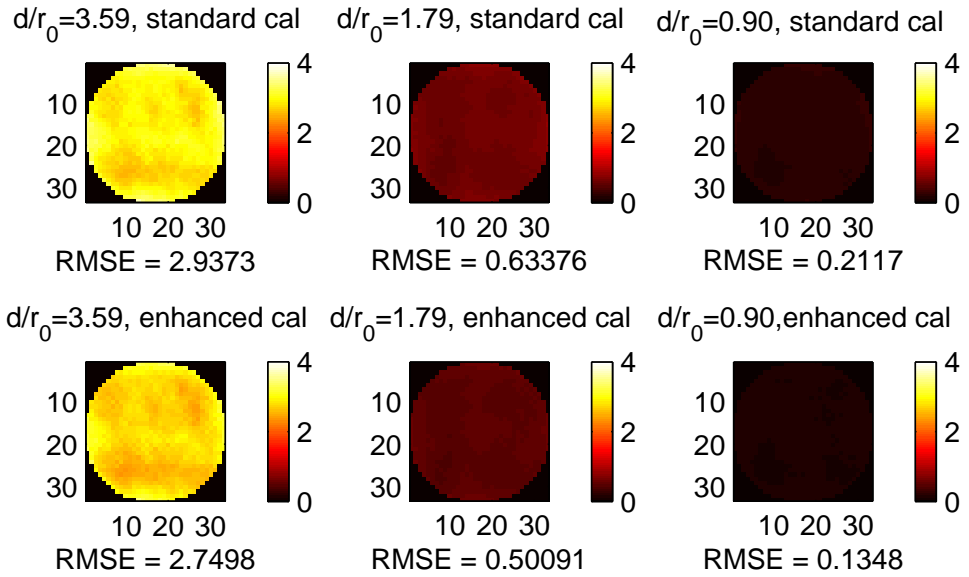


**Figure 31. Full results, ISS path, $4 \times 4$ cell.**
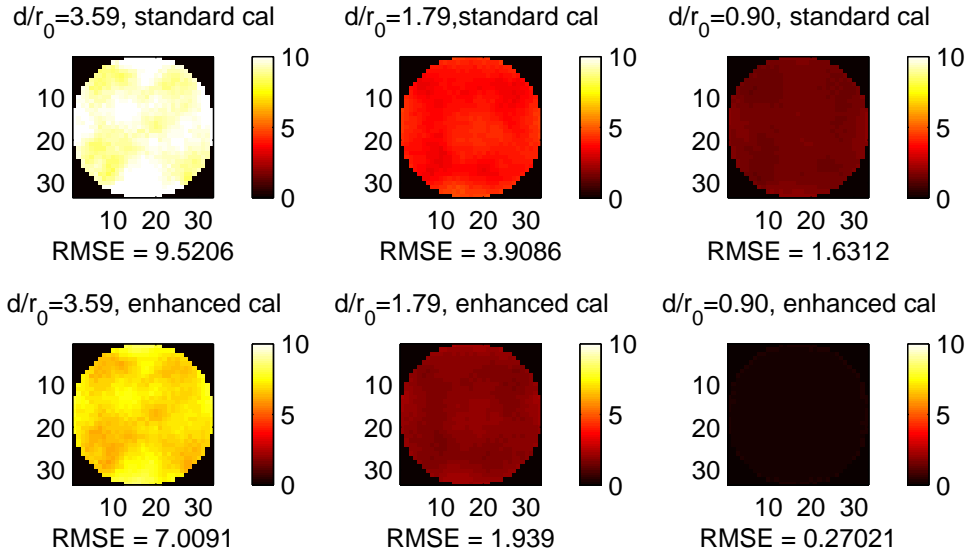
**Figure 32. Full results, GPS path, quad cell.**
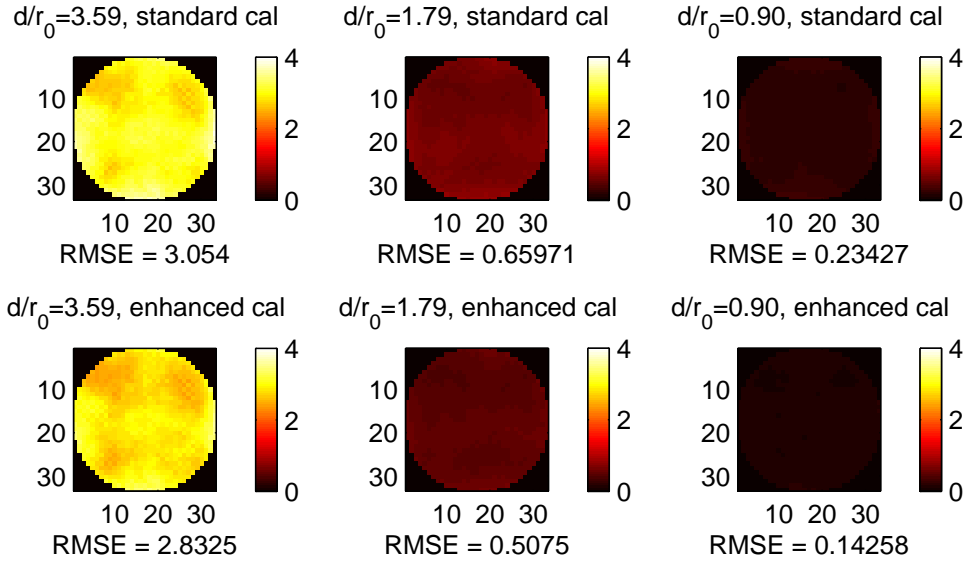


**Figure 33. Full results, GPS path, $4 \times 4$ cell.**

# V. Conclusions and Future Work

This research has developed a model to represent the current AO system at the Starfire Optical Range. Although this model did not consider every aspect that affects the AO system, including all hardware specifications and noise sources, it still demonstrated the improvement in measurement capability that can be achieved by considering Coudè rotation and perspective elongation.

This chapter outlines some of the areas that would require improvement before this model could be implemented into a current system, and also some of the interesting features that were discovered through the development of this model.

## 5.1 Desired Improvements

The model that was developed was kept flexible in its design to easily compare different scenarios. Some areas of its design were kept generic for simplicity, and require alteration before applying the model to a specific system. For example, the PSF of the real optical equipment should be used to ensure that it correctly matches the system. Similarly, the reconstruction matrix used to convert the wavefront slope measurements into DM commands was developed using AOTools and fits the data onto a $33 \times 33$ actuator DM. The actual reconstruction matrix for the real DM should be used in its place. Also, the AO system components were modeled as being ideal, and there was no accounting for the spatial influence function due to neighboring actuators on the DM.

The resolution of the beacon images at each subaperture was chosen to be $64 \times 64$ grid points, as a compromise between the time it took to run each simulation and the quality of the results. This was chosen due to the large number of test cases that were analyzed, but this resolution should be improved to achieve more

accurate results once the system has been modeled correctly. Additionally, the beacon images themselves are merely approximations, and further analysis into the effects of perspective elongation, such as experimental data, is essential to provide a closer fit to real effects. Other techniques such as image correlation may be a suitable option to account for the elongation.

Finally, implementing this model in a laboratory would be of tremendous benefit in validating the model. Unfortunately, realistic laboratory sized extended beacons are not currently available.

## 5.2  Implementation

If this model was to be implemented, it is unlikely that improved calibration factors could be determined in real-time using current computer processing capabilities. To overcome this, two methods could be implemented. The first would require pre-calculating calibration factors using the predicted trajectory of the object to be viewed. This would be relatively simple to implement, but would require a new calibration model for each trajectory. This could be done either between satellite passes if there is sufficient time or earlier in the day once the nightly target list has been determined.

An alternate solution could be to run the model for fixed positions in azimuth and elevation to cover one quarter of the visible sky, as shown in Fig. 34. The remaining sky would be determined by rotating the $x$ and $y$ axes of the original measurement. Provided a sufficient number of points are analyzed in the space, the remaining calibration factors could be interpolated from nearby measurements. It is expected that these calibration factors could be accessed in real-time scenarios, and would only require measurements during the initial implementation of this technique.
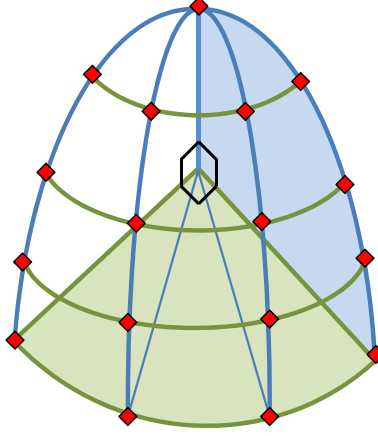
**Figure 34. Quadrant of the sky showing an example of how calibration could be determined at specific azimuth-elevation angles and interpolated for angles between these points.**

## 5.3    Key Results

This research effectively showed that using standard calibration techniques in the presence of elongated references sources introduces inaccuracies in wavefront measurement. The model developed through this research predicts that errors in the reconstructed phase can be reduced by up to 50% by correctly predicting the shape of the measured Shack-Hartmann spot.

Factors such as $d/r_0$ were characterized, revealing that smaller values of $d/r_0$ produced less errors in the reconstructed phase, which is expected. This was a useful technique to verify the model. Additionally, the effect of detector resolution was investigated, and again the results matched expectations. This research determined that improving the detector from a quad cell to a $4 \times 4$ pixel detector improved results more than by simply accounting for the source elongation during sensor calibration. It is expected that this greater improvement will come with a much greater financial cost, in addition to the complexity associated with its implementation.

One surprising result is the location of phase error. Despite the gradient measurements visibly being most inaccurate at subapertures affected by the greatest per-

spective elongation, this did not relate to the greatest phase errors being present at these locations after phase reconstruction. Analysis of the location of the phase error relevant to distance from the laser indicated that there was little to no correlation between phase measurement error and distance to laser.

One possible explanation for this is that the results were obtained using a tilt-removed reconstructor, whereas there may still be some residual tilt present in the wavefront, even after being corrected by a FSM. This removal of tilt may mask the location of errors.

## 5.4 Future Work

Further work on this model is highly encouraged, and recommendations on how to improve the model are provided in this section. These include incorporating the enhanced calibration factors into the reconstruction matrix, replacing the beacon image with a more realistic image, and adjusting atmospheric parameters with telescope orientation.

### 5.4.1 Dynamic Reconstructor.

In the current implementation of the model, measured wavefront slopes are multiplied by their respective calibration factors and then reconstructed using Eq. (17). A slight variation of this method would be to post-multiply the reconstructor matrix $\mathsf{H}$ with the matrix form of the calibration factors, $\mathsf{C}$, such that

$$\phi = \mathsf{HCs}. \tag{26}$$

Despite achieving the same results, performing this operation would allow analysis of the effect of elongation and pupil rotation on the new reconstruction matrix $\mathsf{HC}$, and

could possibly be a precursor to developing a predictive and dynamic reconstruction matrix.

### 5.4.2  Improved Beacon Image.

Another improvement that could be readily implemented involves replacing the first-order approximation of the beacon image described by Eq. (22) with a more realistic image. The beacon image could be created by considering the three-dimensional nature of the sodium layer, including the varying diamter of the laser beam as it propagates and the Gaussian distribution of sodium atoms within the layer. The image could be modeled using multiple two-dimensional slices through the sodium layer, and the resulting beacon propagated to the telescope using wave optics software. Furthermore, the calibration method using the Gaussian approximation could remain unchanged to characterize the sensitivity of the results in this research to changes in the shape of the beacon.

### 5.4.3  Varying Atmospheric Parameters.

In this model, the same $C_n^2$ profile and therefore $r_0$ value was used to model atmospheric turbulence, regardless of the elevation angle of the telescope. This was done to characterize sensor performance at varying elevation angles due to beacon elongation and rotation separately from the effects of varying atmospheric parameters. A more realistic model would adjust the turbulence parameters with the elevation angle of the telescope.

## 5.5  Impact of Work

The cumulative effect of pupil rotation and perspective elongation on wavefront sensor measurements is a unique issue affecting the Starfire Optical Range. Despite

currently performing well, the system could still be improved by simply implementing the methods outlined in this thesis. Although once more complex factors are considered, the actual reduction in RMSE of the measured phase may not be as great as determined by this model ($\approx$50%), a definite improvement is still achievable.

# Appendix A.  MATLAB Code

**Listing A.1. performance.m**

```matlab
function [EnhCal StdCal] = performance(nloops, r0fac, PIXres, az, el)
%PERFORMANCE determines the measurement error for standard and
%enhanced calibration methods with LGS elongation.
% Designed to run several test cases with various r0 values and
%detector resoltions. Produces EnhCal and StdCal, the error using
%each random phase screen compared against an ideal system.
%NOTE: Results are straight differences between ideal reconstructed
%phase and the two calibration methods. Further analysis such as
%taking the root mean square, and/or averaging over the active
%subapertures (877 for 32x32) must still be performed!
%NOTE: Don't forget to generate H, the reconstruction matrix from the
%subapdlg toolbox!!
%
% @author:  FLTLT Russell McGuigan
% @date:    21Feb2011
% @inputs:
%   nloops: number of random phase screen draws
%   r0fac:  factor to alter r0 (for comparisons)
%   PIXres: detector resolution (e.g. 2 for 2x2 quad cell)
%   az/el:  azimuth/elevation angles [rad]
% @outputs:
%   EnhCal: error of enhanced calibration method
%   StdCal: error of standards calibration method
%%%%%%%%%%%%%%%%%%%%%%%%%%%%%%%%%%%%%%%%%%

%%%%%%%%%%%%%%%%%%%%%%
% Initial Setup
```

```matlab
28  %%%%%%%%%%%%%%%%%%%%%%
29  Diameter=   3.5;%Telescope diameter, [m]
30  Nsub=        32; %Number of subapertures across telescope
31  L_sep=       1;  %radial separation of laser from edge of telescope,[m]
32  theta_0=     0;  %initial offset of Coude path [deg]
33
34  r0=0.061*r0fac; %Fried's parameter
35  N=2^10;          %Resolution of phase screen
36  PSFres=64;       %resolution of PSF and Ellipse image
37
38  myPath = myTrack(az,el);    %generate track data
39  myLayer  = myLayers(myPath);%determine distance to sodium layer
40  %boundaries for given track data
41  myTelescope = myTel( Nsub,Diameter,L_sep,[], PIXres, theta_0);
42  %generates subaperture grid
43  myLaser=myC_rotate(myTelescope,myPath);
44  %Determines Coude rotation for a given
45  %path and telescope
46  myTurb = myAtmosphere(Nsub,Diameter,r0,N);
47  %Generates random phase screen
48  PSFwidth=1;               %Determines width of sinc^2 function
49  [PSF eta nu]=myPSFgen(myTelescope,PSFres,PSFwidth);
50  %Generates PSF for a given system
51  minor_ax=0.1;             %Width of ellipse minor axis
52  res=8;                    %factor to upsample calibration data
53  %to achieve smooth curves
54  shiftfac=0.09*PSFres/32;   %Factor to translate images due to
55  %local tilt. Similar effect to
56  %changing the speed of a lens
57
58  %%%%%%%%%%%%%%%%%%%%%%%%%%%%%%
59  %% Standard Calibration
```

```matlab
60  %%%%%%%%%%%%%%%%%%%%%%%%%%%%%%%%
61  calpos=[-15:3:15];           %radian range to calibrate sensor over
62  myLayer2=myLayer;            %reproduce layer values, used to
63  myLayer2.Mean=0;             %produce a 'null' ellipse for standard
64  %calibration
65  for xcal=1:length(calpos);   %determines centroid of each input
66      ycal=0;                  %translates in x direction only
67      ellipse=myEllipseGen(myLaser,1, myTelescope.x(1,1),...
68          myTelescope.y(1,1),eta, nu, myLayer2,0.005,1,...
69          calpos(xcal),ycal,shiftfac);
70      %generate ellipse for one subaperture.
71      %based on telescope/target parameters
72      convolved_ellipse=conv2(PSF,ellipse);
73      %convolves ellipse and PSF
74      cutoff=round(0.25*length(convolved_ellipse));
75      %determines excess padding to remove
76      conv_ellipse4=convolved_ellipse(cutoff:3*cutoff,...
77          cutoff:3*cutoff);    %remove padding from convolution
78      integrated_convolved=myInt(conv_ellipse4,myTelescope.res);
79      %integrate images over detector pixels
80      %(effectively determines photocounts)
81      sum_tot=sum(sum(integrated_convolved)); %total photocounts
82      nocal_x(xcal)=sum(sum(integrated_convolved.*...
83          myTelescope.x_loc/sum_tot))/myTelescope.Diameter;
84      %determines centroid of image
85  end
86  vec_x_2a=interp(nocal_x,res);%interpolates measurements for a
87  %smooth cal curve
88  vec_x_2=vec_x_2a(1:end-res+1);%removes final values for same axis
89  %plotting
90  steps2=length(vec_x_2);      %determines length of cal curve
91  x_ax_2=linspace(calpos(1),calpos(end),steps2);%used to aligns cal
```

59

```matlab
92   %curve to input value
93   mid=round(length(vec_x_2)/2);%determines centre cal point
94   rng=round(0.07*length(vec_x_2));%determines range over which to
95   %fit linear region (0.07= +and-7%)
96   test_x=polyfit(x_ax_2(mid-rng:mid+rng),vec_x_2(mid-rng:mid+rng),1);
97   %fit linear polynomian (line) to curve
98   nocal_x2=test_x(1);        %takes gradient of line as cal factor
99   nocal_y2=nocal_x2;         %x and y are symmetric
100  %%%%%%%%%%%%%%%%%%%%%%%%%%%%%%%%%%%%%%%%%%%%%%%%%%%%%%%%%
101  %% Enhanced Calibration
102  %%%%%%%%%%%%%%%%%%%%%%%%%%%%%%%%%%%%%%%%%%%%%%%%%%%%%%%%%
103  %Performs same calibration as standard cal, but generates a
104  %unique beacon images at each subaperture to model actual
105  %measurements
106  for x_pos = 1:Nsub          %Perform for all subapertures
107      for y_pos = 1:Nsub      %(within mask)
108          if (myTelescope.mask(x_pos,y_pos)>0)
109              for xcal=1:length(calpos);
110                  ycal=0;
111                  ellipse=myEllipseGen2(myLaser,...
112                      1, myTelescope.x(x_pos,y_pos),...
113                      myTelescope.y(x_pos,y_pos),eta, nu,...
114                      myLayer,minor_ax,1,calpos(xcal),ycal,...
115                      shiftfac);%generate unique ellipse
116                  convolved_ellipse=conv2(PSF,ellipse);
117                  cutoff=(0.25*length(convolved_ellipse));
118                  conv_ellipse4=convolved_ellipse(ceil(cutoff):...
119                      floor(3*cutoff),ceil(cutoff):...
120                      floor(3*cutoff));
121                  integrated_convolved=myInt(conv_ellipse4,...
122                      myTelescope.res);
123                  sum_tot=sum(sum(integrated_convolved));
```

```matlab
124             mycal_x(xcal)=sum(sum(integrated_convolved.*...
125                 myTelescope.x_loc/sum_tot))...
126                 /myTelescope.Diameter;
127         end
128         for ycal=1:length(calpos) %x and y cals will differ
129             xcal=0;
130             ellipse=myEllipseGen2(myLaser,...
131                 1, myTelescope.x(x_pos,y_pos),...
132                 myTelescope.y(x_pos,y_pos),...
133                 eta, nu, myLayer,minor_ax,1,...
134                 xcal,calpos(ycal),shiftfac);
135             convolved_ellipse=conv2(PSF,ellipse);
136             cutoff=(0.25*length(convolved_ellipse));
137             conv_ellipse4=convolved_ellipse(ceil(cutoff):...
138                 floor(3*cutoff),ceil(cutoff):...
139                 floor(3*cutoff));
140             integrated_convolved=myInt(conv_ellipse4,...
141                 myTelescope.res);
142             sum_tot=sum(sum(integrated_convolved));
143             mycal_y(ycal)=sum(sum(integrated_convolved.*...
144                 myTelescope.y_loc/sum_tot))...
145                 /myTelescope.Diameter;
146         end
147         vec_x_2a=interp(mycal_x,res);
148         vec_x_2=vec_x_2a(1:end-res+1);
149         vec_y_2a=interp(mycal_y,res);
150         vec_y_2=vec_y_2a(1:end-res+1);
151         steps2=length(vec_x_2);
152         x_ax_2=linspace(calpos(1),calpos(end),steps2);
153
154         mid=round(length(vec_x_2)/2);
155         rng=round(0.1*length(vec_x_2));
```

```matlab
156            test_x=polyfit(x_ax_2(mid-rng:mid+rng),...
157                vec_x_2(mid-rng:mid+rng),1);
158            test_y=polyfit(x_ax_2(mid-rng:mid+rng),...
159                vec_y_2(mid-rng:mid+rng),1);
160            cal_x(x_pos,y_pos)=test_x(1);%store cal factor
161            cal_y(x_pos,y_pos)=test_y(1);
162        else
163            cal_x(x_pos,y_pos)=0;
164            cal_y(x_pos,y_pos)=0;
165        end
166    end
167 end
168 %%%%%%%%%%%%%%%%%%%%%%%%%%%%%%%%%%%%%%%%
169 %% Apply a random phase screen to score performance
170 %%%%%%%%%%%%%%%%%%%%%%%%%%%%%%%%%%%%%%%%
171 load H   %load reconstructor matrix from subapdlg toolbox
172         %must have pre saved and contain ActiveSubs and
173         %Active acts. Run toolbox and use command:
174         %'save H H H0tlt ActiveActs ActiveSubs'
175 H=H0tlt;%Use tilt removed reconstructor
176 EnhCal=zeros([nloops,Nsub+1,Nsub+1]);%pre-allocate result arrays
177 StdCal=zeros([nloops,Nsub+1,Nsub+1]);
178 for idxprime=1:nloops %perform for each iteration
179    phz=myTurb.phase; %extract phase screen data
180    phz_ds=interp2(phz,linspace(1,N,Nsub+1),...
181        transpose(linspace(1,N,Nsub+1)));
182            %downsample phase screen for display, if required
183    steps=round(linspace(1,length(phz),Nsub+1));
184    screen_grad_x=myTurb.screen_grad_x; %extract gradient values
185    screen_grad_y=myTurb.screen_grad_y;
186
187    mask=logical(ActiveActs);%converts matrix to logicals
```

```matlab
188     S=[screen_grad_y(ActiveSubs); screen_grad_x(ActiveSubs)];
189         %creates ideal slope matris
190     P=zeros(size(ActiveActs)); %initialise reconstructed phase
191     P(mask)=H*S; %Rreconstructs phase
192
193     mycentroid_x=zeros([Nsub,Nsub]); %initialise centroid values
194     mycentroid_y=zeros([Nsub,Nsub]);
195     for x_pos = 1:Nsub  %perform centroiding for each subaperture
196         for y_pos = 1:Nsub
197             if (myTelescope.mask(x_pos,y_pos)>0)
198                 ellipse=myEllipseGen2(myLaser,...
199                     1, myTelescope.x(x_pos,y_pos),...
200                     myTelescope.y(x_pos,y_pos),eta, nu,...
201                     myLayer,minor_ax,1,...
202                     screen_grad_x(x_pos,y_pos),...
203                     screen_grad_y(x_pos,y_pos),shiftfac);
204                     %generates beacon image, shifted depending on
205                     %turbulence gradient
206                 convolved_ellipse=conv2(PSF,ellipse);
207                 cutoff=round(0.25*length(convolved_ellipse));
208                 conv_ellipse4=convolved_ellipse(cutoff:...
209                     3*cutoff,cutoff:3*cutoff);
210                 integrated_convolved=myInt(conv_ellipse4,...
211                     myTelescope.res);
212                 sum_tot=sum(sum(integrated_convolved));
213                 mycentroid_x(x_pos,y_pos)=sum(sum(...
214                     integrated_convolved.*...
215                     myTelescope.x_loc/sum_tot))...
216                     /myTelescope.Diameter;
217                 mycentroid_y(x_pos,y_pos)=sum(sum(...
218                     integrated_convolved.*...
219                     myTelescope.y_loc/sum_tot))...
```

63

```matlab
220                     /myTelescope.Diameter;
221             else
222                     mycentroid_x(x_pos,y_pos)=0;
223                     mycentroid_y(x_pos,y_pos)=0;
224             end
225         end
226     end
227
228     mycentroid_x_n=mycentroid_x./nocal_x2;%apply standard
229     mycentroid_y_n=mycentroid_y./nocal_y2;%calibration factor
230     mycentroid_x=mycentroid_x./cal_x;%apply enhanced calibration
231     mycentroid_y=mycentroid_y./cal_y;%factor
232
233     S_m=[mycentroid_y(ActiveSubs); mycentroid_x(ActiveSubs)];
234     P_m=zeros(size(ActiveActs));
235     P_m(mask)=H*S_m;    %reconstruct enhaced cal phase
236
237     S_n=[mycentroid_y_n(ActiveSubs); mycentroid_x_n(ActiveSubs)];
238     P_n=zeros(size(ActiveActs));
239     P_n(mask)=H*S_n;    %reconstruct standard cal phase
240
241     temp1(:,:)=P-P_m;   %take difference between real and
242                        %enhanced cal phase values
243     temp2(:,:)=P-P_n;   %take difference between real and
244                        %standard cal phase values
245     EnhCal(idxprime,:,:)=temp1; %save result for each iteration
246     StdCal(idxprime,:,:)=temp2;
247                %results still need analysis, and to be RMSE'd
248 end
249 end
```

**Listing A.2. myEllipseGen.m**

```matlab
function [ellipse] = myEllipseGen( Laser, time, x, y,...
    eta,nu, myLayer,minor_ax,A , x_grad,y_grad,shift)
%MYELLIPSEGEN generates quassian beacon for a given system
%orientation.
% Eliiptical shape depends on the location of the subaperture
% and laser, local tilt on the wavefront, speed of the lenslet,
% sodium layer dimensions and look angle
%
% @author:  FLTLT Russell McGuigan
% @date:    21Feb2011
% @inputs:
%   Laser:      Structure containing laser Coude rotation info
%   time:       position along track (if multiple az/el angles
%               defined), should be 1 for single position
%   x/y:        subaperture geometry [m]
%   eta/nu:     grid on which image is formed
%   myLayer:    sodium boundary information
%   minor_ax:   Ellipse minor axis (fixed)
%   A:          Ellipse max intensity (usually 1)
%   x_grad:     local x tilt over subaperture
%   y_grad:     local y tilt over subaperture
%   shift:      amount that tilt affects spot displacement,
%               similar to speed or focal length of lenslet
% @outputs:
%   ellipse:    Gaussian (elliptical looking) beacon image
%               which depends on all the above inputs
%%%%%%%%%%%%%%%%%%%%%%%%%%%%%%%%%%%%%%%%%%%

theta_rel2 = atan2(Laser.beacon_y(time)-y,...
    Laser.beacon_x(time)-x);
%Calculate distance and angle to laser from each subaperture
```

```
32  dist_rel=sqrt((Laser.beacon_x(time)−x).^2+...
33      (Laser.beacon_y(time)−y).^2);
34  %Calculate ground distance from subaperture to
35  %top and bottom of LGS
36  theta_width=atan2(myLayer.High(time),dist_rel)−...
37      atan2(myLayer.Low(time),dist_rel);
38  %calculate angular width of LGS and convert to distance
39  theta2=theta_width*myLayer.Mean(time);
40  theta2=max(theta2,minor_ax);
41  %ensures that the width is never less than the minor axis
42  %width
43  x_offset=x_grad*shift*cos(theta_rel2)−...
44      y_grad*shift*sin(theta_rel2);
45  %coordinate transformation to rotate ellipse offset
46  %to align with beacon
47  y_offset=x_grad*shift*sin(theta_rel2)+...
48      y_grad*shift*cos(theta_rel2);
49  eta2=eta*cos(theta_rel2)−nu*sin(theta_rel2);
50  %coordinate transformation to rotate ellipse
51  %to align with beacon
52  nu2=eta*sin(theta_rel2)+nu*cos(theta_rel2);
53  ellipse = 1*exp(−((eta2−x_offset).^2/(2*theta2)+...
54      (nu2−y_offset).^2/(2*minor_ax)))*A;
55  %generate actual ellipse
56  end
```

**Listing A.3. Miscellaneous Functions**

```
1  function [ myPath ] = myTrack( az,el )
2  %MYTRACK converts azimuth and elevation angle data into a
3  %single structure and converts from degrees to radians
```

```matlab
4   %
5   % @author:  FLTLT Russell McGuigan
6   % @date:    21Feb2011
7   % @inputs:
8   %   az:       telescope azimuthal angle [deg]
9   %   el:       telescope elevation angle [deg]
10  % @outputs:
11  %   myPath: structure storing az and el data [rad]
12  %%%%%%%%%%%%%%%%%%%%%%%%%%%%%%%%%%%%%%%%%%%
13  if length(az)~=length(el);  %basic length check to ensure
14                                  %a value wasn't missed
15      disp('Azimuth and Elevation data must be same length')
16  else
17      for idx=1:length(az);
18          myPath.el(idx)=el(idx)*pi/180;%convert to radians
19          myPath.az(idx)=az(idx)*pi/180;
20      end
21  end
22
23  end
24
25  function [ Layers ] = myLayers( Path, Low, High, wvl, R )
26  %MYLAYERS Determines high low and mean boundary heights for
27  %a given satellite look angle
28  %
29  % @author:  FLTLT Russell McGuigan
30  % @date:    21Feb2011
31  % @inputs:
32  %   Path:   telescope track data (az and el) [rad]
33  %   Low:    sodium layer lower boundary at zenith [m]
34  %   High:   sodium layer upper boundary at zenith [m]
35  %   wvl:    sodium laser wavelength [m]
```

```matlab
36  %   R:       Earth radius [m]
37  % @outputs:
38  %   Layers: structure containing boundary height info
39  %%%%%%%%%%%%%%%%%%%%%%%%%%%%%%%%%%%%%%%%%

40
41  if nargin <5    %generic earth radius if not specified
42          R=6371000;
43  end
44  if nargin<4     %sodium wavelength (if not specified)
45      wvl=589.2e-9;
46  end
47  if nargin==1;   %zenith boundary heights (if not specified)
48      Low=85000;
49      High=95000;
50  end
51  Layers.R=R;     %stores earth radius and laser wavelength
52  Layers.wvl=wvl;
53  Layers.High=Layers.R*cos(pi/2+Path.el)+...
54      sqrt((High+Layers.R)^2-(Layers.R*sin(pi/2+Path.el)).^2);
55                  %Distance to top boundary layer, assuming
56                  %spherical earth
57  Layers.Low=Layers.R*cos(pi/2+Path.el)+...
58      sqrt((Low+Layers.R)^2-(Layers.R*sin(pi/2+Path.el)).^2);
59                  %Distance to lower boundary layer
60  Layers.Mean=0.5*(Layers.High+Layers.Low);%Layer midpoint
61  end
62
63  function [Telescope]=myTel(Nsub,Diameter,L_sep,FOV,res,theta_0)
64  %MYTEL Stores telescope data into a single structure and
65  %generates detector geometry
66  %
67  % @author:  FLTLT Russell McGuigan
```

```matlab
68  % @date:    21Feb2011
69  % @inputs:
70  %   Nsub:       Number of telescope subapertures
71  %   Diameter:   Telescope diameter [m]
72  %   L_sep:      radial separation of laser from edge of
73  %               telescope [m]. Put −Diameter/2 for centre
74  %               launched
75  %   FOV:        Telescope FOV (no longer used)
76  %   res:        detector resolution. 2 for quad cell
77  %   theta_0:    initial Coude offset of exit pupil [deg]
78  % @outputs:
79  %   Telescope:  structure containing telescope information
80  %               ans subaperture and detector geometries
81  %%%%%%%%%%%%%%%%%%%%%%%%%%%%%%%%%%%%%%%%%
82
83  Telescope.Nsub=Nsub; %stores data into structure
84  Telescope.Diameter=Diameter;
85  Telescope.L_sep=L_sep;
86  Telescope.FOV=FOV;
87  Telescope.res=res;
88  Telescope.theta_0=theta_0*pi/180;%convert offset to radians
89  x=(−Nsub/2+1/2:1:Nsub/2−1/2)*Diameter/Nsub;
90                  %generate subaperture geometry
91  [x y]=meshgrid(x);
92  Telescope.x=x;
93  Telescope.y=y;
94  Telescope.mask=double(x.^2+y.^2<=(Diameter/2)^2);
95                  %generate subaperture mask
96  x_loc=Diameter/2*((−(res−1)/res):2/res:((res−1)/res));
97                  %generate detector geometry
98  [Telescope.x_loc Telescope.y_loc] = meshgrid(x_loc);
99  end
```

```
100

101  function [ atmosphere ] = myAtmosphere(Nsub,Diameter,r0,N)

102  %MYATMOSPHERE generates random phase screen, calculates its

103  %gradient.

104  %

105  % @author:  FLTLT Russell McGuigan

106  % @date:    21Feb2011

107  % @inputs:

108  %   Nsub:       Number of telescope subapertures

109  %   Diameter:   Telescope diameter [m]

110  %   r0:         Atmospheric coherence diamter (Fried's

111  %               parameter [m]

112  %   N:          Number of grid points across phase screen

113  % @outputs:

114  %   atmosphere: structure containing phase screen values

115  %               and average gradients over each subaperture

116  %%%%%%%%%%%%%%%%%%%%%%%%%%%%%%%%%%%%%%%%%%

117

118  PHZ=kolmogphzscreen(N,Diameter,r0,0,[0 0],randi(10000));

119      %generates phase screen for given parameters. no added

120      %tilt

121  phz=PHZ.phase;

122  steps=round(linspace(1,length(phz),Nsub+1));

123      %determines locations over which to average gradients

124  atmosphere.screen_grad_x=zeros(Nsub); %initialis gradients

125  atmosphere.screen_grad_y=atmosphere.screen_grad_x;

126  for idx1=1:Nsub %loop for each subaperture

127      for idx2=1:Nsub

128        sub_screen=phz(steps(idx1):steps(idx1+1),...

129            steps(idx2):steps(idx2+1));

130          %sub divide phase screen into subapertures

131        [fx,fy]=gradient(sub_screen); %compute gradients for
```

70

```matlab
132           %each subaperture
133        atmosphere.screen_grad_x(idx1,idx2)=mean(mean(fx));
134           %average the gradient over the subaperture (x and y)
135        atmosphere.screen_grad_y(idx1,idx2)=mean(mean(fy));
136      end
137 end
138 atmosphere.phase=phz;   %store phase values
139 end
140
141 function [ PSF eta nu] = myPSFgen( Telescope, res,a )
142 %MYPSFGEN generates diffraction limited spot
143 %
144 % @author:  FLTLT Russell McGuigan
145 % @date:    21Feb2011
146 % @inputs:
147 %   Telescope:  Structure containing telescope data
148 %   res:        number of grid points for PSF generation
149 %   a:          width of PSF
150 % @outputs:
151 %   PSF:        sinc^2 diffraction limited
152 %   eta:        cartesian grid of x values on which the
153 %               PSF lies
154 %   nu:         eta's y value equivalent
155 %%%%%%%%%%%%%%%%%%%%%%%%%%%%%%%%%%%%%%%%%
156
157 eta=linspace(-1.75,1.75,res); %initialise sensor grid
158 [eta nu] = meshgrid(eta);
159 PSF=sinc(a*eta).^2.*sinc(a*nu).^2;
160      %generate PSF (sinc^2) function
161 end
162
163 function [ Laser ] = myC_rotate( Telescope, Track)
```

```matlab
%MYC_ROTATE determines the Coude rotation of the laser
%beacon and it's x and y position
%
% @author:  FLTLT Russell McGuigan
% @date:    21Feb2011
% @inputs:
%   Telescope:  Structure containing telescope data
%   Track:      Structure containing target azimuth
%               and elvation values in radians
% @outputs:
%   Laser:      Coude angle and position of laser
%%%%%%%%%%%%%%%%%%%%%%%%%%%%%%%%%%%%%%%%%%

Laser.theta_beac=Track.az-Track.el+Telescope.theta_0;
    %determine Coude rotation
Laser.beacon_x=(Telescope.Diameter/2+Telescope.L_sep)...
    *cos(Laser.theta_beac);%determine laser x location
Laser.beacon_y=(Telescope.Diameter/2+Telescope.L_sep)...
    *sin(Laser.theta_beac);%determine laser y location
end
```

# Bibliography

[1] Andrews, Larry C. and Ronald L. Phillips. *Laser Beam Propagation through Random Media*. SPIE Press, Bellingham, WA, 2nd edition, 2005.

[2] Béchet, C., M. Tallon, I. Tallon-Bosc, E. Thiébaut, M. Le Louarn, and R. M. Clare. "Optimal Reconstruction for Closed-Loop Ground-Layer Adaptive Optics with Elongated Spots". *J. Opt. Soc. Am. A*, 27(11), Nov 2010.

[3] Beckers, J. M. "Overcoming Perspective Elongation Effects in Laser-Guide-Star-Aided Adaptive Optics". *Appl. Opt.*, 31(31), Nov 1992.

[4] Beckers, Jacques M., Mette Owner-Petersen, and Torben Andersen. "A rapid refocussing system for the Euro50 telescope aimed at removing the perspective elongation of laser beacons". *SPIE Proc.*, 5169, 2003.

[5] Brennan, T. J. and P. H. Roberts. *AOTools User's Guide*. the Optical Sciences Company, 2008.

[6] Brennan, T. J., P. H. Roberts, and D. C. Zimmerman. *WaveProp User's Guide*. the Optical Sciences Company, 2008.

[7] Brennan, T. J. and J. D. Schmidt. *Personal Communication*. 2008.

[8] Drummond, J. "2006 Summary of 50 W Fasor Sky Tests and Model Summary". *Technical Report*, Starfire Optical Range, 2006.

[9] Fried, D. L. and G. E. Mevers. "Evaluation of $r_0$ for Propagation Down Through the Atmosphere". *Appl. Opt.*, 13:2620–2622, Nov 1974.

[10] Goodman, Joseph W. *Introduction to Fourier Optics*. Roberts and Company, Inc., Greenwood Village, CO, 2005.

[11] Hardy, John W. *Adaptive Optics for Astronomical Telescopes*. Oxford University Press, New York, NY, 1998.

[12] Hecht, Eugene. *Optics*. Pearson Education, Upper Saddle Rive, NJ, 2002.

[13] Hubbard, R. "Image Rotation at the Gregorian and Coudé Positions for the Alt-Azimuth Telescope". *ATST Technical Note 0012*, 2005.

[14] Jeys, T. "Development of a Mesospheric Sodium Laser Beacon for Atmospheric Adaptive Optics". *Lincoln Laboratory Journal*, 4(2):133–149, 1991.

[15] Johnson, R., D. Montera, T. Schneeberger, and J. Spinhirne. "A New Sodium Guidestar Adaptive Optics System for the Starfire Optical Range 3.5m Telescope". *Technical Report*, The Boeing Company, May 2009.

[16] Kibblewhite, E. J. *Laser Guide Star Adaptive Optics for Astronomers*, volume 551 of *C*. Kluwer Academic Publishers, Dordrecht, The Netherlands, 2000.

[17] Mateen, M., D. Sanchez, T. Rhoadarmer, L. Arguella, D. Oesch, D. Fung, R. Petty, P. Kelly, R. Vincent, and J. Richey. "Adaptive Optics with the deformable mirror not in pupil: Part I. Experimental Results". *Proc. SPIE*, 7093, 2008.

[18] NASA. "Human Space Flight SkyWatch 2.0". *http://spaceflight.nasa.gov/realdata/sightings/SSapplications/Post/JavaSSOP/ JavaSSOP.html, NASA, 18 Oct*, 2010.

[19] Quirrenbach, A. *Laser Guide Star Adaptive Optics for Astronomers*, volume 551 of *C*. Kluwer Academic Publishers, Dordrecht, The Netherlands, 2000.

[20] Schmidt, Jason D. *Numerical Simulation of Optical Wave Propagation*. SPIE Press, Bellingham, WA, 2010.

[21] Shtyrkova, K., M. D. Oliker, K. P. Vitayaudom, D. W. Oesch, D. J. Sanchez, P. R. Kelly, C. M. Tewksbury-Christle, and J. C. Smith. "Experimental Demonstration of Real Time Gradient Gain Correction for Sodium Beacon Laser Guide Star". *Technical Paper*, DEPS, 2010.

[22] Thomas, S., T. Fusco, A. Tokovinin, M. Nicolle, V. Michau, and G. Rousset. "Comparison of Centroid Computation Algorithms in a Shack Hartmann Sensor". *Mon. Not. R. Astron. Soc.*, 371:323–336, 2006.

[23] Trimble. "Trimble Planning Software". *http://www.trimble.com/ planningsoftware.shtml, Trimble, 16 Feb*, 2010.

[24] Viard, Elise, Franoise Delplanckea, Norbert Hubin, and Nancy Ageorges. "LGS Na-spot elongation and Rayleigh scattering effects on Shack-Hartmann wavefront sensor performances". *SPIE Proc.*, 3762(8), 1999.

[25] Vitayaudom, Kevin P., Darryl J. Sanchez, Denis W. Oesch, Patrick R. Kelly, Carolyn M. Tewksbury-Christle, and Julie C. Smith. "Experimental analysis of perspective elongation effects using a laser guide star in an adaptive-optics system". *SPIE Proc.*, 7466, 2009.

[26] Website, Keck Observatory. "Keck Obsevatory". *http://www2.keck.hawaii.edu/optics/ lgsao/images/031117acam7.png, Keck, 16 Feb*, 2010.

[27] Website, United States Air Force. "Images". *www.af.mil/images, 21 Feb*, 2010.

[28] Website, United States Air Force. "Starfire Optical Range Fact Sheet". *http://www.kirtland.af.mil/library/factsheets/factsheet.asp?id=15868, 21 Feb*, 2010.

# REPORT DOCUMENTATION PAGE

The public reporting burden for this collection of information is estimated to average 1 hour per response, including the time for reviewing instructions, searching existing data sources, gathering and maintaining the data needed, and completing and reviewing the collection of information. Send comments regarding this burden estimate or any other aspect of this collection of information, including suggestions for reducing this burden to Department of Defense, Washington Headquarters Services, Directorate for Information Operations and Reports (0704–0188), 1215 Jefferson Davis Highway, Suite 1204, Arlington, VA 22202–4302. Respondents should be aware that notwithstanding any other provision of law, no person shall be subject to any penalty for failing to comply with a collection of information if it does not display a currently valid OMB control number. **PLEASE DO NOT RETURN YOUR FORM TO THE ABOVE ADDRESS.**

| 1. REPORT DATE *(DD–MM–YYYY)* | 2. REPORT TYPE | 3. DATES COVERED *(From — To)* |
|---|---|---|
| 24–03–20111 | Master's Thesis | Aug 2009 — Mar 2011 |

**4. TITLE AND SUBTITLE**

EFFECT OF COUDÉ PUPIL ROTATION ON SODIUM LASER BEACON PERSPECTIVE ELONGATION

**5a. CONTRACT NUMBER**

**5b. GRANT NUMBER**

F2KBAC0006G001

**5c. PROGRAM ELEMENT NUMBER**

**6. AUTHOR(S)**

Russell J. McGuigan, FLTLT, RAAF

**5d. PROJECT NUMBER**

ENGJON163

**5e. TASK NUMBER**

**5f. WORK UNIT NUMBER**

**7. PERFORMING ORGANIZATION NAME(S) AND ADDRESS(ES)**

Air Force Institute of Technology
Graduate School of Engineering and Management (AFIT/EN)
2950 Hobson Way
WPAFB OH 45433-7765

**8. PERFORMING ORGANIZATION REPORT NUMBER**

AFIT/GE/ENG/11-28

**9. SPONSORING / MONITORING AGENCY NAME(S) AND ADDRESS(ES)**

Air Force Research Laboratory)
Darryl J. Sanchez, PhD
3550 Aberdeen Ave SE
Kirtland AFB, NM 87117-5776
(505)846-7209, (DSN: 246-7209), darryl.sanchez@kirtland.af.mil

**10. SPONSOR/MONITOR'S ACRONYM(S)**

AFRL/RDS

**11. SPONSOR/MONITOR'S REPORT NUMBER(S)**

**12. DISTRIBUTION / AVAILABILITY STATEMENT**

APPROVED FOR PUBLIC RELEASE; DISTRIBUTION UNLIMITED.

**13. SUPPLEMENTARY NOTES**

This material is declared a work of the U.S. Government and is not subject to copyright protection in the United States.

**14. ABSTRACT**

This research models a sodium laser guide star and its measurement by a Shack-Hartmann wavefront sensor. By predicting the extent of beacon elongation and Coudé rotation, reference images are produced for each subaperture throughout an engagement scenario. These reference sources are then used to continuously recalibrate the system as it changes orientation. This model measures the effect of perspective elongation and Coudé on SHWFS measurements to quantitatively determine the extent of degradation that occurs.

**15. SUBJECT TERMS**

Adaptive Optics, Perspective Elongation, Laser Guide Star

| 16. SECURITY CLASSIFICATION OF: | | | 17. LIMITATION OF ABSTRACT | 18. NUMBER OF PAGES | 19a. NAME OF RESPONSIBLE PERSON |
|---|---|---|---|---|---|
| a. REPORT | b. ABSTRACT | c. THIS PAGE | | | Jason D. Schmidt, Maj USAF (ENG) |
| U | U | U | UU | 87 | 19b. TELEPHONE NUMBER *(include area code)* (937) 785-3636, x7224; Jason.Schmidt@afit.edu |

Standard Form 298 (Rev. 8–98)
Prescribed by ANSI Std. Z39.18